Publication Year	2020
Acceptance in OA	2025-03-11T15:52:28Z
Title	Spectral Signatures of Chromospheric Condensation in a Major Solar Flare
Authors	Graham, David R., CAUZZI, Gianna, ZANGRILLI, Luca, Kowalski, Adam, Simões, Paulo, Allred, Joel
Publisher's version (DOI)	10.3847/1538-4357/ab88ad
Handle	http://hdl.handle.net/20.500.12386/36675
Journal	THE ASTROPHYSICAL JOURNAL
Volume	895

The Astrophysical Journal, 895:6 (22pp), 2020 May 20 https://doi.org/10.3847/1538-4357/ab88ad

Spectral Signatures of Chromospheric Condensation in a Major Solar Flare

David R. Graham[1], Gianna Cauzzi[2,3], Luca Zangrilli[4], Adam Kowalski[2,5,6], Paulo Simões[7,8], and Joel Allred[9]
[1] Bay Area Environmental Research Institute, Moffett Field, CA 94035, USA
[2] National Solar Observatory, University of Colorado Boulder, 3665 Discovery Drive, Boulder, CO 80303, USA; gcauzzi@nso.edu
[3] INAF-Osservatorio Astrofisico di Arcetri, I-50125 Firenze, Italy
[4] INAF-Osservatorio Astrofisico di Torino, I-10025 Pino Torinese, Italy
[5] Department of Astrophysical and Planetary Sciences, University of Colorado, Boulder, 2000 Colorado Avenue, CO 80305, USA
[6] Laboratory for Atmospheric and Space Physics, University of Colorado Boulder, 3665 Discovery Drive, Boulder, CO 80303, USA
[7] Centro de Rádio Astronomia e Astrofísica Mackenzie, Escola de Engenharia, Universidade Presbiteriana Mackenzie, Brazil
[8] SUPA School of Physics and Astronomy, G12 8QQ, University of Glasgow, UK
[9] NASA/Goddard Space Flight Center, Code 671, Greenbelt, MD 20771, USA
Received 2019 November 6; revised 2020 April 7; accepted 2020 April 9; published 2020 May 19

Abstract

We study the evolution of chromospheric line and continuum emission during the impulsive phase of the X-class SOL2014-09-10T17:45 solar flare. We extend previous analyses of this flare to multiple chromospheric lines of Fe I, Fe II, Mg II, C I, and Si II observed with the Interface Region Imaging Spectrograph, combined with radiative-hydrodynamical (RHD) modeling. For multiple flaring kernels, the lines all show a rapidly evolving double-component structure: an enhanced emission component at rest, and a broad, highly redshifted component of comparable intensity. The redshifted components migrate from 25 to 50 km s^{-1} toward the rest wavelength within ~30 s. Using Fermi hard X-ray observations, we derive the parameters of an accelerated electron beam impacting the dense chromosphere, using them to drive an RHD simulation with the RADYN code. As in Kowalski et al. (2017), our simulations show that the most energetic electrons penetrate into the deep chromosphere, heating it to $T \sim 10{,}000$ K, while the bulk of the electrons dissipate their energy higher, driving an explosive evaporation, and its counterpart condensation—a very dense ($n_e \sim 2 \times 10^{14}$ cm^{-3}), thin layer (30–40 km thickness), heated to 8–12,000 K, moving toward the stationary chromosphere at up to 50 km s^{-1}. The synthetic Fe II 2814.45 Å profiles closely resemble the observational data, including a continuum enhancement, and both a stationary and a highly redshifted component, rapidly moving toward the rest wavelength. Importantly, the absolute continuum intensity, ratio of component intensities, relative time of appearance, and redshift amplitude are sensitive to the model input parameters, showing great potential as diagnostics.

Unified Astronomy Thesaurus concepts: Solar flares (1496); Solar chromosphere (1479); Solar activity (1475); Radiative transfer simulations (1967); Solar ultraviolet emission (1533)

1. Introduction

Solar flares bear on multiple aspects of plasma physics, including the physics of magnetic reconnection, the transport of energy from the corona to the lower atmosphere, the production of coronal mass ejections driving space weather, etc. (Shibata & Magara 2011; Benz 2017). The solar flare paradigm remains widely accepted as a template for magnetic activity on other stars (e.g., Namekata et al. 2017), thus a full understanding of the phenomenon is highly relevant for astrophysics in general.

In particular, the chromosphere remains a crucial element for understanding the development of flares. While the primary energy release mechanism is governed by magnetic reconnection in the corona, the chromosphere is the location where this energy is ultimately deposited, either via conduction or accelerated particles; this gives rise to the largest contribution to the flare radiative output (Fletcher et al. 2011; Milligan et al. 2014), and, via chromospheric evaporation, to the necessary mass and energy to fill the flaring loops with plasma at temperatures in excess of 10 MK (Fisher et al. 1985).

After a long period of relative neglect, the past decade has seen a renewed interest in the chromospheric response to flares. This has been driven partly by the availability of novel instrumentation, such as the imaging spectro-polarimeters IBIS (Cavallini 2006) and CRISP (Scharmer et al. 2008), as well as the recent Interface Region Imaging Spectrograph (IRIS, De Pontieu et al. 2014), which has been used in numerous flare studies. On the other hand, building on the pioneering work of Fisher and colleagues in the 1980s (Fisher et al. 1985; Fisher 1987, 1989; Neidig & Machado 1986), several groups have developed radiative-hydrodynamical (RHD) simulations that aim at understanding the effects of a strong and sudden heating burst affecting the lower solar atmosphere (Allred et al. 2005, 2015; Reep et al. 2015; Rubio da Costa et al. 2015b; Heinzel et al. 2016). The complexities of fully accounting for hydrodynamical (including the presence of shocks) and radiative transfer effects in determining the chromosphere's response to flaring limit the simulations to the 1D case only; this is usually well justified by the control that magnetic fields exert to plasma dynamics, however (see, e.g., Allred et al. 2015; Rubio da Costa et al. 2015b).

The flaring chromospheres resulting from the models can then be compared with proper observational diagnostics to gauge their realism; most often, this is accomplished using radiative transport codes such as RH (Uitenbroek 2001) to synthesize relevant chromospheric lines (including the resonance lines of Mg II h&k, Ca II H&K, or Hα) in snapshots of the simulations' output, to provide a direct comparison with observables. Some of the relevant mechanisms influencing the formation of these strong, optically thick chromospheric spectral lines in flaring conditions remain an active subject of study, including the effects of partial frequency redistribution for the Mg II resonance lines (Kerr et al. 2019a) or the role of enhanced densities on the broadening of the hydrogen Balmer lines (Kowalski et al. 2017b). Still, this method offers the best diagnostic possibilities, especially when the temporal evolution is factored in the comparison because the dynamics of the flaring plasma are extremely sensitive to the details of heating and energy transport (Kerr et al. 2015; Reep et al. 2015, 2016; Kowalski et al. 2017a).

Comparisons of this kind have been attempted many times in the past using strong optical lines (e.g., Canfield et al. 1990; Falchi et al. 1992; Falchi & Mauas 2002), and continued to date with data at much higher spatial resolution and spectral coverage (Kowalski et al. 2015, 2017a, 2019; Kuridze et al. 2015; Rubio da Costa et al. 2016; Heinzel et al. 2017). Still, fully resolved—spatially, temporally, and spectrally—observations of the impulsive phase of flares remain scarce, owing to the difficulty of positioning the slit of a spectrometer exactly at the flare footpoints, and exactly at the time of energy deposition in the lower atmosphere. Because numerical simulations mostly concentrate on the very first instants ($\leqslant 100$ s) of the flare development, comparisons with observations have often been less than optimal.

Recent observations of flare dynamics, obtained at high spatial and temporal resolution with the IRIS spacecraft and other instruments, are improving this situation greatly (Brosius & Inglis 2018; Jeffrey et al. 2018; Tian & Chen 2018; Polito et al. 2019). One of the best examples to date of chromospheric dynamics and condensation during a flare has been presented in Graham & Cauzzi (2015, hereafter Paper I), who exploited a unique sit-and-stare high-cadence (9.4 s) IRIS data set obtained during a strong flare, to reveal clear signatures of chromospheric condensation in multiple footpoint sources. The fortuitous development of the flare along the spectrograph slit allowed the authors to uncover the quantitative similarity of the dynamical behavior of a number of flaring pixels, hinting at the possibility of spatially resolved elementary flare kernels over subarcsecond spatial scales. The use of imaging spectrometers working in the optical range also appears to be very promising: Libbrecht et al. (2019) recently presented results obtained with CRISP, using the He I D_3 line to study the chromospheric dynamics in a small C-class flare. The large field of view (FOV) afforded by the instrument enabled the spatial characterization of condensation motions that were found in the leading edge of ribbons, as previously reported by Falchi et al. (1997, albeit at a much lower spatial and temporal resolution). Furthermore, the condensation is found to decay from its maximum value of $\sim$60 km s^{-1} to zero in about 60 s, a very similar evolution to what has been reported in Paper I using the Mg II 2791.6 Å subordinate line.

An interesting result of Libbrecht et al. (2019) is that the interpretation of their spectropolarimetric He I data in the flaring footpoints requires the use of two separate chromospheric components (“slabs”), one related to the condensation, and the other pertaining to a deeper layer, where the spectral component appears enhanced with respect to quiet conditions, and modestly blueshifted. This second component begins to become visible about one time-step (15 s) after the maximum redshift of the condensation, and has been interpreted by the authors as due to shock heating (and possible rebound) of the undisturbed chromosphere by the moving condensation. A similar scenario has been presented by Kowalski et al. (2017a) using IRIS observation of Fe II lines in flaring kernels: the authors showed that in some instances, these chromospheric spectral lines were clearly composed of two distinct spectral components, one at the rest wavelength and the other strongly redshifted. However, the authors offer a fairly different interpretation than Libbrecht et al. (2019): using RADYN flare simulations (Allred et al. 2015), constrained by the hard X-ray (HXR) observations obtained with RHESSI, they were able to reproduce the observed shapes of the Fe II lines as due to concomitant effects of the energy delivered by a beam of accelerated electrons. In particular, while the low-energy electrons ($E \sim 25$–50 keV) in the beam are responsible for creating the evaporation and heating the chromospheric condensation—producing a strongly redshifted line, the higher energy electrons ($E \geqslant 50$ keV) can penetrate in deeper, denser layers of the chromosphere and heat them, giving rise to the enhanced stationary component. Key to understanding the flaring mechanism itself is the fact that the relative timing and strength of these separate effects depends on the details of the heating input, including the hardness of the beam and the duration of the input.

The IRIS flare studied by Kowalski et al. (2017a) was observed in raster mode with a moderate cadence of 45 s, so that a full study of the temporal evolution of the chromospheric condensation could not be carried out. In the present paper we expand on these findings, using the unique data set of Paper I to study the full temporal evolution of multiple chromospheric lines in multiple flaring kernels during the impulsive phase of the flare, with excellent spectral and temporal resolution. Following Kowalski et al. (2017a), we take advantage of cotemporary HXR data from Fermi (Meegan et al. 2009), as well as the IRIS slit-jaw images (SJIs) to properly estimate the full parameters of the energy input. We further synthesize the Fe II 2814 Å line for comparison with the data; as shown by Heinzel & Kleint (2014) and Kowalski et al. (2017a), this line is an important diagnostic in flares because the intensity originates from a similar temperature range (with a broad peak around $T \sim 12{,}000$ K) as hydrogen Balmer bound–free radiation that dominates the IRIS near-UV (NUV) range.

2. The SOL2014-09-10T17:45, X1.6 Event

The GOES X1.6 class flare SOL2014-09-10T17:45 developed in active region NOAA 12158 near disk center (N15E02). The complex two-ribbon structure encompassed both the western portion of the main leading-polarity sunspot, and a group of several smaller spots of following polarity embedded in the plage, as seen in Figure 1. The flare developed in a bursty manner, with UV kernels of various intensity appearing in rapid succession, in particular, running northeast to southwest along the length of the plage ribbon. At the same time, the ribbons expanded roughly perpendicularly to their length, as in the canonical flare model.

Several authors have by now described many aspects of the flare, including the precursor phase (Zhou et al. 2016), the eruption of a filament and slipping motion of flare loops (Dudík et al. 2016), the presence of quasi-periodic pulsations (Li et al. 2015a; Simões et al. 2015; Ning 2017), and the occurrence of chromospheric evaporation (Li et al. 2015b; Tian et al. 2015) and its relation with chromospheric condensation (Paper I). Representative movies depicting the flare evolution are available in, e.g., Tian et al. (2015) and Dudík et al. (2016).

As discussed in the introduction, the present paper focuses on the chromospheric emission during the flare’s impulsive phase, and its diagnostic potential with respect to radiative-

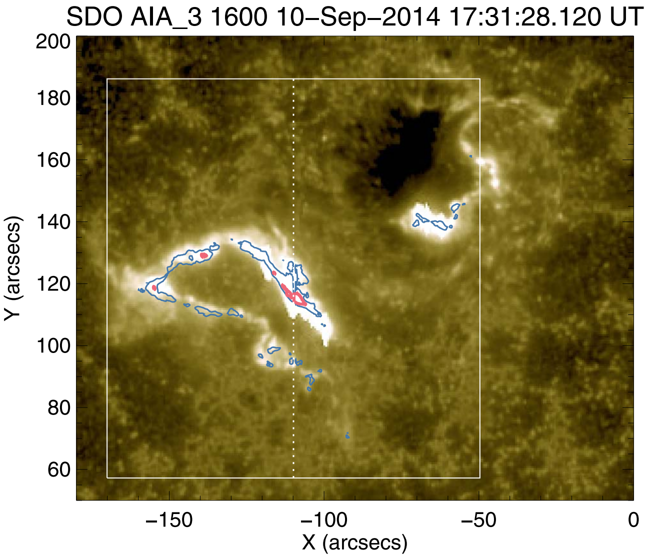

Figure 1. AIA 1600 Å image at maximum flare brightness. Contours in blue show the extent of the ribbon in IRIS 2796 Å at 15% of the maximum SJI intensity, while the brightest kernel is shown in pink, at the 50% intensity level. The thin white box indicates the IRIS SJI FOV, and the dotted line marks the IRIS slit position.

hydrodynamical modeling. To this end, we discuss mostly the HXR observations obtained by Fermi/Gamma-Ray Burst Monitor (GBM; Meegan et al. 2009) and the UV spectra and images acquired by IRIS (De Pontieu et al. 2014), in particular around the time of maximum IRIS UV emission. GOES soft X-ray (SXR) light curves and SDO/AIA images at various wavelengths provide the necessary context.

Figure 2 shows the GOES SXR 1–8 Å flux over most of the event's evolution. A modest increase in the SXR is visible already from about 16:50 UT, but the main impulsive phase starts only after 17:20 UT. The event then develops very rapidly, with the SXR flux peaking already at 17:45 UT. The Fermi GBM count-rate profiles, integrated in the energy bands 6–12, 20–50, 50–100, and 100–300 keV, are shown in Figure 3. While RHESSI was in night-time during most of the flare, Fermi completely covered the impulsive phase, revealing a strong and rapid increase in the 20–300 keV flux, starting from ~17:22 UT and reaching its maximum around 17:36 UT. A second episode of enhanced HXR flux is also observed, between 17:43 UT and 17:50 UT. Further analysis of the Fermi data is provided in Section 4, in particular, for the short time-interval framed by the dashed lines in Figure 3.

A unique set of observations was acquired by IRIS, which was running a flare watch program on NOAA 12158, using the sit-and-stare mode and the standard flare line list (OBSID 3860259453). High-cadence (9.4 s) flare spectra were obtained for many hours before the flare and until the end of the impulsive phase. Several spectral windows were acquired within the 1332–1358 Å, 1389–1407 Å (far-UV, FUV), and 2783–2834 Å (NUV) intervals (see, e.g., Figure 3 in Kowalski et al. 2017a). Exposure times were 8 s for both NUV and FUV channels until the start of the flare; afterward, NUV exposures were reduced to 2.4 s to avoid saturation. Simultaneous SJIs were obtained at a cadence of ~19 s, alternating between two channels: 2796 Å centered on Mg II, and 1400 Å centered on Si IV. The 120″ × 120″ FOV of IRIS is shown as a white box in Figure 1; the IRIS spectrograph slit is indicated with a dotted white line.

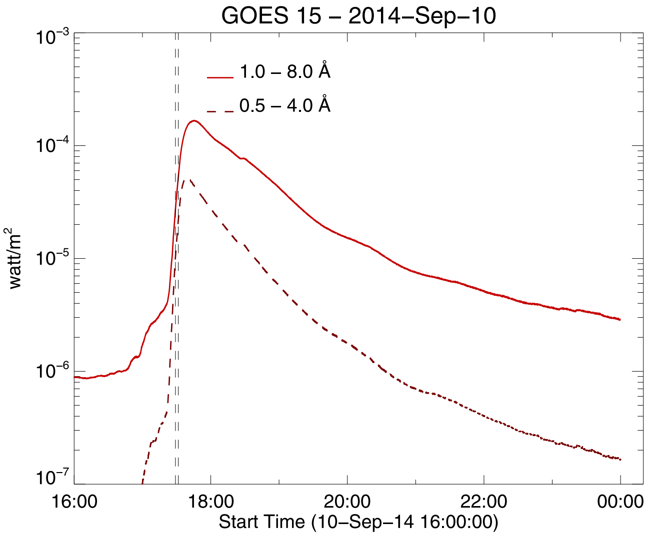

Figure 2. GOES 1–8 Å flux over several hours around the event. The data used in this paper pertain to the very rapid impulsive phase, as framed by the dashed lines.

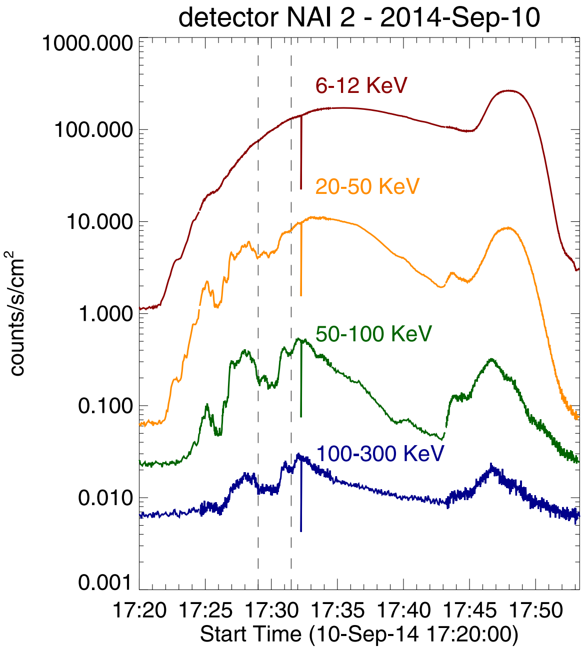

Figure 3. HXR detector count flux of the SOL2014-09-10T17:45 impulsive phase in several of the Fermi GBM energy bands. The dashed lines frame the interval corresponding to the period of maximum UV emission analyzed in the paper.

The peculiarities of the IRIS observations are manyfold: first, the spectrograph slit was positioned exactly over the plage flare ribbon, and among others, intersected the strongest kernel within the whole flare (as observed in the SJIs). Second, the ribbon developed rapidly along the slit, providing multiple independent instances of elementary flaring kernels (see Paper I for a more thorough discussion). Third, the observations started well before the initiation of the flare, thus capturing the evolution of any given flaring area from their earliest moments. This is a very rare occurrence. Fourth, the 9.4 s cadence is among the highest ever achieved for UV flare spectra, and allows novel analyses of the rapidly evolving chromospheric condensation. Finally, the strongest flaring kernels were so intense that many weak chromospheric lines clearly turned into emission, providing a range of complementary diagnostics in addition to the most often used Mg II and C II lines.

Figure 1 shows the flare ribbons at the time of maximum chromospheric emission, as determined from the 2796 Å SJIs. The most intense brightening in the IRIS images is highlighted by a pink contour in the simultaneous AIA 1600 Å image; at this time, the kernel was at maximum brightness and directly sampled by the slit (the kernel can also be identified by the saturated region in Figure 1 of Paper I). The kernel was particularly bright between 17:29:48 and 17:31:41 UT; during this time, its intensity accounted for 15%–20% of the total 2796 Å SJI counts while accounting for only $\sim$1% of the total SJI area. In the following we thus focus on this particular feature by studying its chromospheric spectra and their evolution, as related to the HXR signatures. Given the high cadence of the HXR data and the excellent sampling of IRIS, such a data set is most appropriate to compare with results from hydrodynamical numerical simulations.

3. Chromospheric Dynamics (Condensation)

In addition to the most frequently used Mg II h & k doublet, a multitude of chromospheric lines is found within the IRIS spectral range. Together, they can improve the interpretation of line shapes and shifts in terms of physical parameters of the flaring lower atmosphere.

In Paper I we showed the temporal evolution of chromospheric condensation in elementary flare kernels by analyzing the Mg II 2791.6 Å subordinate line. In particular, we used the position of the line bisector at 30% of the peak intensity level to estimate the amplitude of downflows. Similarly to earlier observations and modeling (e.g., Fisher 1989), condensation velocities of up to 30–40 km s^{-1} were found, rapidly decaying to zero within 30–60 s. While the evolution of the condensation velocity was extremely clear (see Figure 5, Paper I), we did not delve further into details of the line profiles themselves. It was, however, apparent that at several positions and times, the Mg II subordinate line profiles were strongly asymmetric, or even had distinct redshifted components. This property was also noted by Tian et al. (2015) for several Si II lines adjacent to the coronal Fe XXI line, but was not analyzed further.

The presence of “satellite” red-wing components is clearly observed in multiple chromospheric lines, as vividly demonstrated in Figure 4. In the figure we compare the temporal evolution of Fe I 2814.11 Å, Fe II 2813.33 Å & 2814.45 Å, and Mg II 2791.6 Å spectra, acquired in one pixel near the brightest part of the ribbon ($y \simeq 119''$, see, e.g., Figures 1 and 10). After a small rise in intensity shortly after 17:30 UT, a strong impulsive burst is observed at the undisturbed position of the lines, accompanied by a noticeable increase of the continuum level around the Fe lines (the variation of the continuum around the Mg II 2791.6 Å line cannot be clearly appreciated within the small spectral range displayed). At the same time, a separate component appears far in the red wing of all the lines, and rapidly migrates back toward the lines’ centroid over the next 4–5 time steps, i.e., in less than a minute.

The top panel of Figure 4 shows the Fe II and Fe I lines, their behavior is essentially identical. The same pattern occurs for the Mg II subordinate line (middle panel) and is observed with varying clarity in many other pixels and lines (see Figures 5, 6, and Appendix A), so the effect is certainly not due to unidentified lines. Common to all the spectral lines shown in Figure 4 is also a brief ($\sim$30 s) and weak (few km s^{-1}) blueward “rebound” occurring around 17:31:30 UT after the redshifted component has fully migrated back to the rest wavelength. This is commented upon in Section 8.

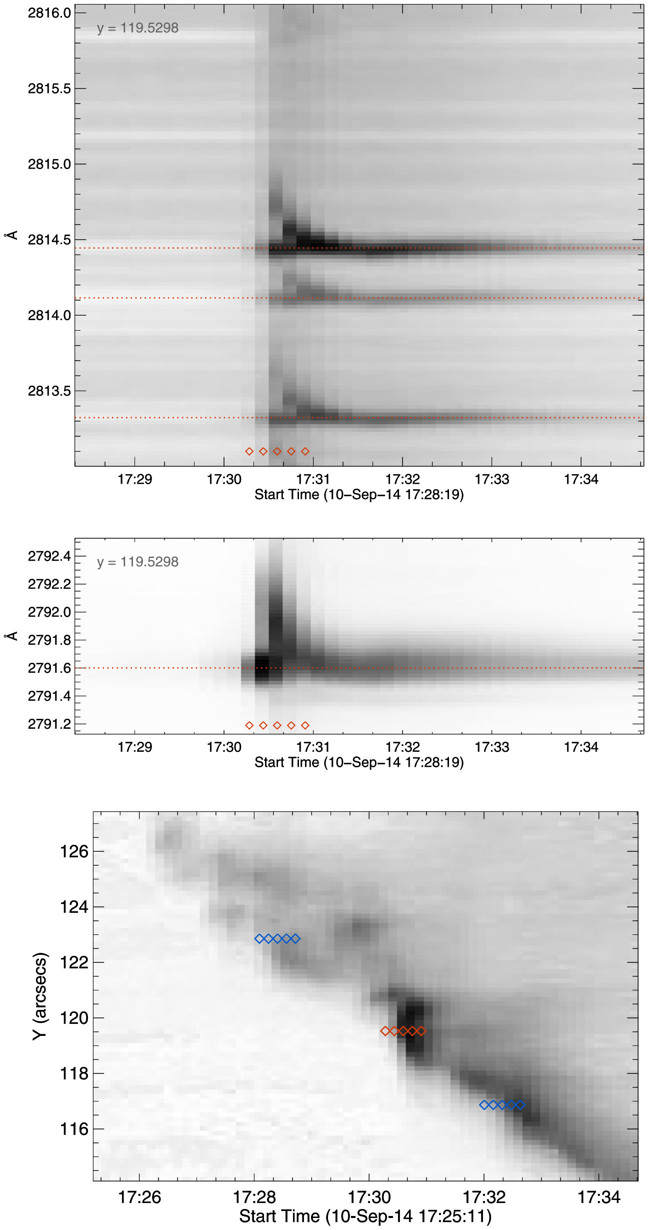

Figure 4. Temporal evolution of Fe I 2814.1 Å and Fe II 2813.33 and 2814.45 Å spectral profiles (top panel) and the Mg II 2791.6 Å subordinate (middle panel) for flaring pixel $y = 119\farcs53$. The intensity scale is reversed for clarity. The presence of a separate rapidly evolving strongly redshifted component is obvious for all lines (horizontal dashed lines mark the rest wavelengths). The red diamonds (all panels) indicate the time of the spectra sampled in Figures 5 and 6. Bottom panel: space–time plot from a subset of 81 pixels along the IRIS slit (see Figure 1 or Paper I for context). The total fitted intensity of the Fe II 2814.45 Å line is shown in the inverted color table. Red diamonds mark the position and times sampled above, while blue diamonds correspond to the spectra in Figures A1–A4.

3.1. Condensation: Spectral Fits

In the following we identify the Fe I 2814.11 Å, Fe II 2813.3 and 2814.45 Å, Mg II 2791.6 Å, C I 1354.284 Å, and Si II 1348.545 Å lines as excellent diagnostics of flare

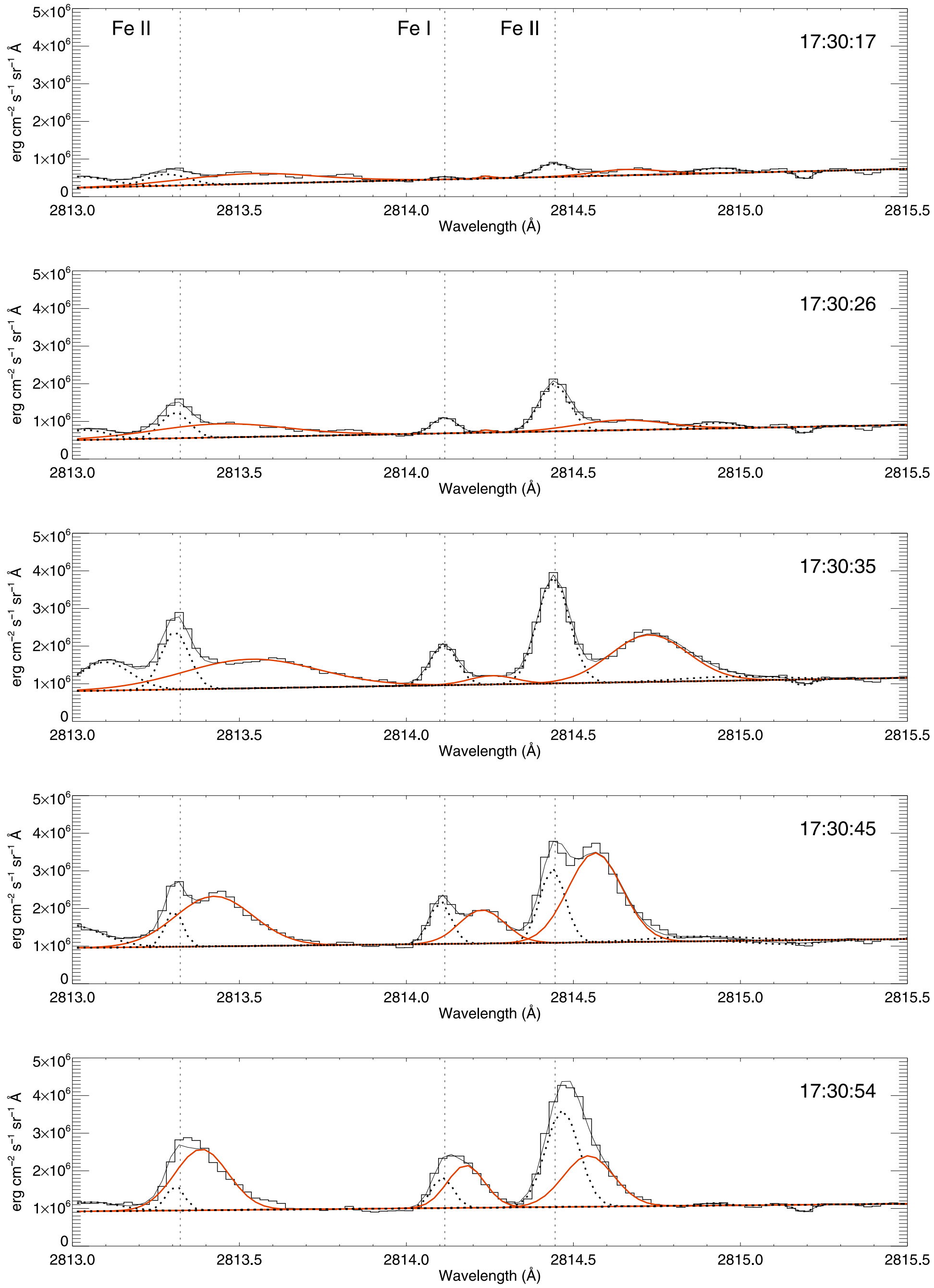

Figure 5. Temporal evolution of the spectra in the Fe II window for multiple chromospheric lines (stepped black lines) for the $y = 119\farcs53$ slit pixel (see markings in Figure 1). The dotted vertical line represents the rest wavelength for each line (labeled in the top panel). Dashed black lines represent the Gaussian fits for the stationary component; red lines the fit for the redshifted components, and the total fit is given as a solid black line. Note that the Gaussian fits are displayed at the native resolution of the IRIS spectra. Time runs vertically, corresponding to the red diamonds in Figure 4 (successive exposures at the overall 9.4 s cadence; 2.4 s exposure). The intensity scale is kept constant to better appreciate the variations in brightness during the flare. No subtraction of preflare background has been performed.

chromospheric dynamics: while their intensity is much enhanced during the flare, these lines remain relatively narrow and unsaturated, and can be fairly well isolated from spectral blends and the general background.

Using the pixel at $y = 119\farcs53$ (marked with red diamonds in the bottom panel in Figure 4) as a particularly clear example, we show in Figure 5 the spectra of multiple chromospheric lines in the Fe II and Fe II window, obtained at five consecutive time steps (stepped black lines). Figure 6 shows the spectra of the Mg II, C I, and Si II lines in the same pixel and times. The times in the panels of Figures 5 and 6 correspond to the red diamonds of Figure 4, and the dotted black line indicates the nominal rest wavelength of each line. The wavelength scale was established by fitting the photospheric Ni I 2799.474 Å line over a 3 hr period before the flare to remove the residual orbital oscillation as described in the IRIS technical note ITN20. We also use the procedure described in IRIS technical note ITN24[10] to convert the raw DN output into intensity, as was done, e.g., by Kleint et al. (2016) and

---

[10] The IRIS technical notes can be found at http://iris.lmsal.com/documents.html.

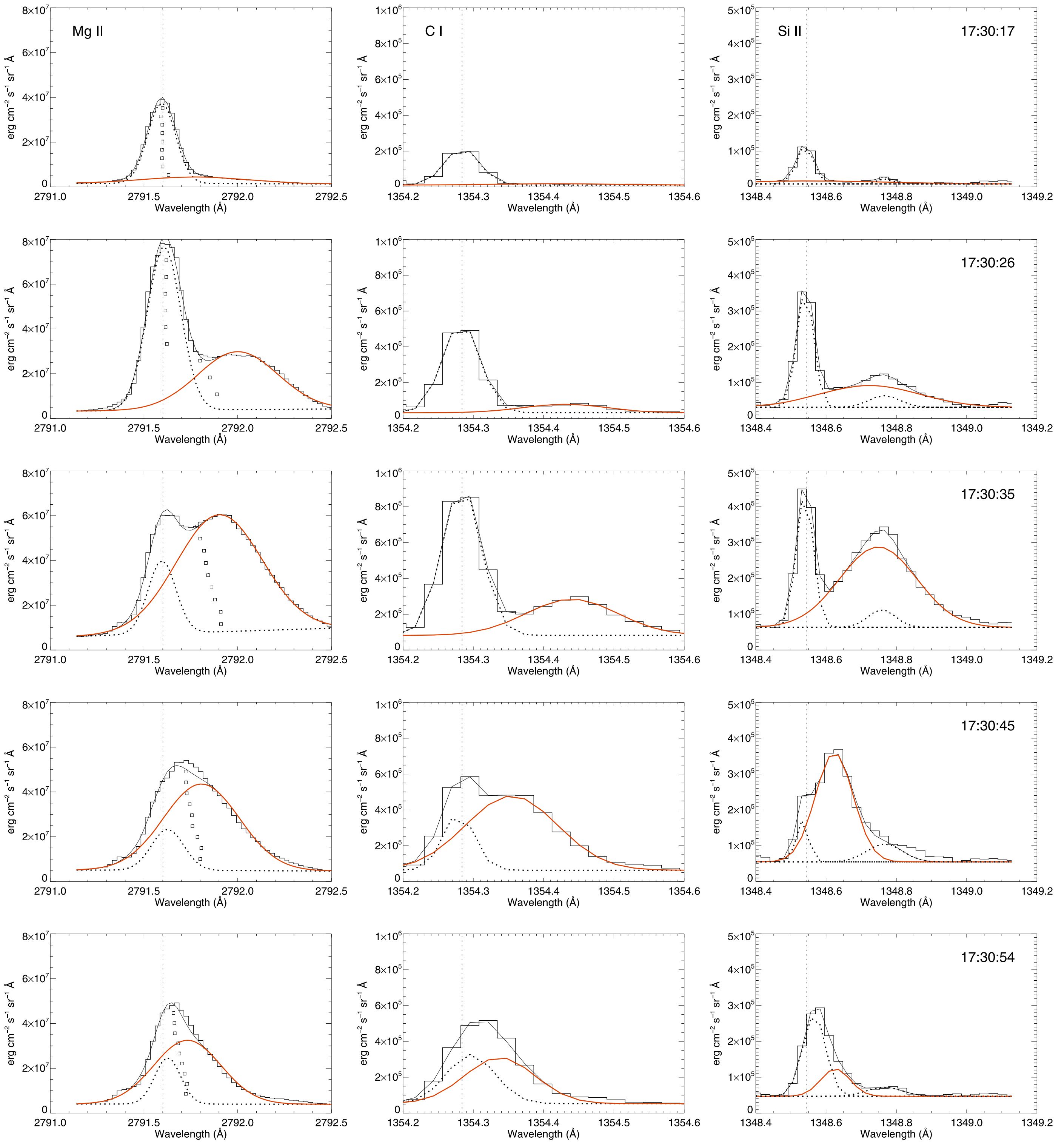

Figure 6. Spectra for the same spatial pixel as described in Figure 5, but for the Mg II, C I, and Si II lines. Note that a 2.4 s exposure was used for Fe II and Mg II, and a 8 s one for Si II and C I. Again, the intensity scale is kept constant for each line. Squares mark the bisectors of the observed Mg II spectra at 10% intensity increments (see Figure C1 and the discussion in Appendix C).

Kowalski et al. (2017a). No subtraction of preflare background has been performed.

In Figures 5 and 6 we see that all lines show a strong intensity increase at 17:30:26 (second row), with a concomitant broad satellite component appearing at high redshifts. The shifted component is weaker at first detection, but in the next two time steps, its intensity becomes comparable with that of the main peak, which remains mostly stationary. While increasing in intensity, the redshifted component rapidly migrates toward the rest wavelength, so that by 17:30:54 (only 37 s from the "preflare" time) the general appearance is that of a single broad asymmetric line. It is worth noting that the redshifted component is more prominent in the Mg II spectra (Figure 6), and can often be unambiguously detected in them one time-step ahead of the other lines (see also the figures in Appendix A). This is probably due to the much higher opacity of this line with respect to the other chromospheric signatures.

Most of the flaring pixels display a behavior similar to that shown in Figures 5 and 6, with spectral profiles very asymmetrical during their early activation, which is due to the presence of the satellite component, and a clear continuum enhancement from the preflare value that is best observed in the Fe II window. As an example, in Appendix A we show corresponding figures for two additional pixels ($y \sim 117''$ and $y \sim 123''$ along the slit); these same pixels are identified with the blue diamonds in Figure 4.

To characterize the dynamics of the condensation, we have thus fit the profiles of each flaring pixel with a pair of Gaussian profiles. Because the shifted component is so prominent, a Gaussian fit should provide a better estimate of the redshift over the traditional bisector method that we employed in Paper I, which we find can slightly underestimate the maximum shift (in Appendix C we make a side-by-side comparison of both techniques.) The weak spectral lines such as Fe II and Fe I are most likely optically thin (see the discussion in Kowalski et al. 2017a, and Section 6 below), so the use of a Gaussian approximation is further justified. For stronger lines, such as the Mg II 2791.6 Å, we follow the original work of Ichimoto & Kurokawa (1984) in assuming that the flare emission originates mostly from a separate optically thin slab of (moving) plasma overlaying the stationary atmosphere. In Figures 5 and 6, the quasi-stationary component of each spectral line is shown with dotted black lines, while the redshifted component is displayed in red. The final overall fit is given as a thin black line. We constrain the central component in all lines to remain within ± 2 km s^{-1} of the rest wavelength, allowing the second shifted component to return as far as possible toward the line rest wavelength, and track its complete velocity evolution. At times, the spectral range in proximity of Fe II 2813.3 Å can be subject to some ambiguities due to the presence of other much weaker Fe I and Fe II lines, but the fits are satisfactory overall. The same problem occasionally affects the fits for the Si II line (Figure 6) as the result of an unidentified weak line that is visible in the later exposures around 1348.75 Å. Its profile remains low in the red wing of the Si II line, so we constrain the maximum intensity and position to avoid double fitting the shifted satellite Si II line (see, e.g., the list of adjacent spectral lines in Sandlin et al. 1986). The stationary component of Si II also has a tendency to peak just blueward of the rest wavelength during the rise phase. The profile is itself slightly asymmetric, perhaps indicating an unidentified blend not listed in the Sandlin et al. (1986) atlas or a difference in the formation height of the ion compared to the other lines shown. Except for these small uncertainties, the general behavior remains very clear in all lines.

Last, we note that the width of the redshifted components appears to be very large with respect to that of the stationary component and to the preflare situation in general. While some broadening might be expected due to the long exposure times coupled with the rapid motion of the component (particularly in the FUV), it is plausible that most of the excess width might be created by flare-induced turbulent motions in the chromosphere (Milligan 2011; Rubio da Costa et al. 2015a); the fact that the width of the redshifted component seems to decrease with time (see the top and bottom panels in Figure 6) might support this interpretation.

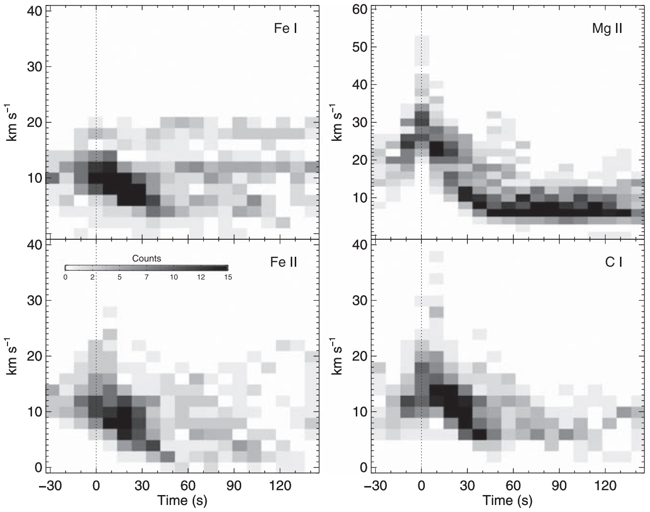

Figure 7. Superposed-epoch analysis of chromospheric condensation flows derived from the second component of the IRIS line fits. The velocity curve for each pixel is aligned in time to the occurrence of maximum centroid shift for the second component of Mg II at that pixel. The velocity indicates downflow motions, and the strength of the color table dictates the number of instances within a 2 km s^{-1} velocity interval for each time-step.

3.2. Condensation: Time Evolution

We now focus on the dynamics displayed by multiple flaring pixels, in particular, those comprising the ribbon between the $y = [114'', 127'']$ positions in Figure 4. These are the same pixels as we analyzed in Paper I.

Using the fits described in Section 3.1, we derive the centroid of the second shifted Gaussian component for each line, pixel, and time-step. The velocity scale for each line is obtained with respect to the rest wavelength shown in Figures 5 and 6. To remove fits where the velocity determination might be biased by nearby lines or low signal, we discarded the fits when the total intensity of the shifted component was below 30% of the maximum reached in any given pixel. This also removes some of the influence of the instrumental point-spread function (PSF) described in Appendix B.

To find commonalities in the flow evolution of the different pixels and lines, we perform a superposed-epoch analysis in analogy to Paper I by aligning the velocity–time curve for each pixel and spectral line to a common zero time. The latter is defined as the time at which maximum shift of the second component in Mg II is reached for any given pixel. Figure 7 displays the resulting curves. For each time-step (given by the cadence of the observations, 9.4 s), the number of pixels within a 2 km s^{-1} interval is represented by the gray scale. The bar in the figure gives the number of pixels within each time–velocity bin.

From Figure 7 we can immediately confirm that the behavior described in Section 3.1 is common to the majority of the flaring pixels in the ribbon sampled by the IRIS slit. While clearest for the Mg II line, the evolution of the redshifted component for all considered pixels and spectral lines falls within a fairly narrow envelope, starting at a maximum redshift of up to 50 km s^{-1}, and rapidly decaying to a rest velocity within 30–60 s. This confirms and expands our previous findings (see Figure 5 in Paper I): the "satellite" component of chromospheric lines provides a clear picture of the condensation occurring within each flaring pixel at the early stages of the flare. The overall decay curve is essentially identical in all lines, even when the spectra in the IRIS FUV and NUV ranges are acquired with different exposure times (8 s and 2.4 s, respectively). Thus, it seems that the 9.4 s cadence of the observations is rapid enough to preserve the basic properties of the condensation evolution (Fisher 1989; Kowalski et al. 2017a), although higher cadence data could provide further insight.

After ∼60 s from the peak velocity, the fits for the redshifted component in most lines become ambiguous, and a large scatter is thus observed in the time–velocity plot. For the Mg II line, a fit is instead possible for a longer period, and a fairly constant condensation velocity of a few km s^{-1} is observed for several minutes (not fully shown in Figure 7).

Finally, from Figure 7 we see that a "buildup phase" of the flows is apparent in Mg II, and possibly in other lines, 1–2 time steps before the peak. This corresponds to the presence of a weak redshifted component for the Mg II line that can be observed earlier than for other lines (see the top panels of Figures 6, A2 and A4). It is difficult to say, however, whether this is due to a difference in opacity between the lines or to some artifact of the PSF (see Appendix B).

4. HXR Spectra

Modern RHD models of the flaring lower solar atmosphere such as the flare RADYN code (Allred et al. 2015) usually assume that the flare energy is transported from the corona by means of a beam of accelerated mildly relativistic electrons. The parameters characterizing the electrons beam can be derived by analyzing the HXR spectra originating from the flaring atmosphere, assuming that the bremsstrahlung emission derives from the impact of such a beam onto the dense chromosphere (e.g., Brown 1971).

To this end, we analyzed the HXR data acquired by the Fermi/GBM. As mentioned in Section 2, Fermi fully covered the impulsive phase of the flare. GBM continuously observes the whole unocculted sky, recording two different data types: CTIME data, with a fine time resolution (0.256 s; 64 ms on flare trigger), but a coarse spectral resolution in eight energy channels; and CSPEC data, with lower time resolution (4.096 s; 1.024 s on flare trigger) and a spectral resolution of 128 energy channels over the 8 keV–1 MeV spectral region. In the following we use CSPEC data, acquired with the NaI02 detector, which was the most favorably oriented one of the 12 sodium iodide (NaI(Tl)) scintillation detectors.

The count-rate profiles integrated in four energy bands are shown in Figure 3 and are briefly discussed in Section 2. The flare was so strong that the 1 s cadence spectra have a high signal-to-noise ratio, so we can reliably derive the HXR spectral parameters at this high temporal resolution. An example of a single Fermi spectrum acquired during the maximum of the flare is given in Figure 8.

Assuming that the bremsstrahlung emission originates in a cold thick-target (Brown 1971), we deduce the accelerated electrons' energy spectrum as characterized by the total flux of nonthermal electrons, a power-law index δ, and a low value of cutoff energy, E_c, of the electron energy distribution. The parameters characterizing the low-energy, thermal component are the electron temperature and the emission measure.

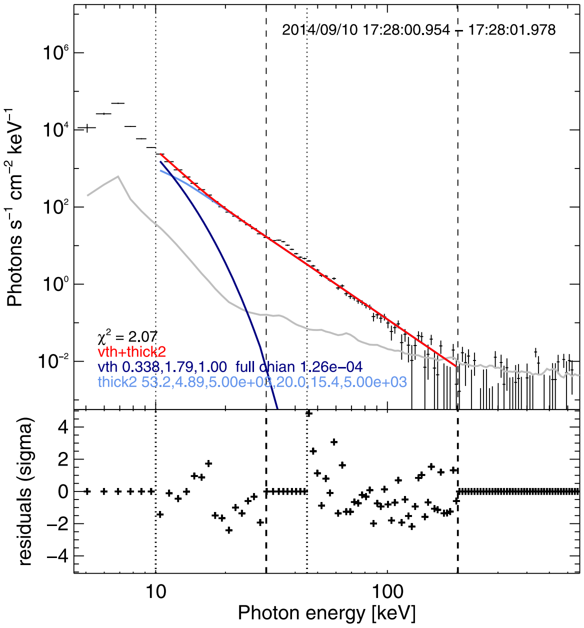

Figure 8. Top panel: HXR spectrum around the time of flare maximum, from Fermi-CSPEC data (black points with error bars). In gray we plot the preflare background flux averaged between 17:13 and 17:15 UT. The colored curves represent the fit obtained from the OSPEX forward-fitting procedure, including a thermal component (dark blue), a single power-law component (light blue), and the combined fit (red). Dotted and dashed lines indicate the lower and upper limits of the two energy ranges used for the nonthermal component fit (10–30 keV and 45–200 keV); this is necessary because of calibration issues that affect the intermediate energies (see the text). Bottom panel: the residuals between the fitted distribution and real data, normalized to the 1σ uncertainty for each respective data point. The fitted distribution can be considered acceptable because most of the points lie within 2σ.

The total nonthermal electron power is calculated using the following relation (Holman et al. 2011):

$$\begin{aligned} P_{n\mathrm{th}} &= k_\mathrm{E} \int_{E_c}^{+\infty} E_0 \mathcal{F}_0(E_0) dE_0 \\ &= \frac{k_E A}{\delta - 2} E_c^{-\delta+2} \ \mathrm{erg\ s^{-1}}, \end{aligned} \quad (1)$$

where $\mathcal{F}_0$ is the injected electron beam flux distribution, E_c is the low-energy cutoff, δ is the spectral index of the electron energy distribution, k_E is the conversion from keV into erg, and A is the normalization factor of the electron flux distribution. The total nonthermal electron energy input in the flare can be estimated by integrating $P_{n\mathrm{th}}$ over the flaring time interval.

The data analysis and the fitting procedure have been performed with the OSPEX routines of the SolarSoft package (Schwartz et al. 2002). Because the Fermi/GBM data have a known calibration issue at the iodine K-edge energy of 33.17 keV, resulting in a discontinuity in the response of the NaI detectors in the case of bright bursts (Bissaldi et al. 2009), we have conservatively excluded the 30–45 keV range from the fits. This is indicated with the dotted and dashed lines in Figure 8.

We have also opted to exclude an albedo component in the fit, although this might be significant in the HXR spectra because the flare is located close to disk center (Santangelo et al. 1973). However, several assumptions that enter the possible albedo contribution, in particular, the pitch-angle distribution function of the nonthermal electrons and the absence of any magnetic mirroring effects (Kontar et al. 2006; Dickson & Kontar 2013), are not independently verifiable. The most relevant contribution of the albedo component is expected in the range ~15–50 keV (Santangelo et al. 1973; Kontar et al. 2006), i.e., overlapping the 30–45 keV range that we excluded from the fit because of the instrumental effects mentioned above. We thus feel that our choice is justified, and note that the results of the fit including the albedo contribution would only potentially decrease the total number of nonthermal electrons by a factor of about 3 (Simões & Kontar 2013), which is well within our final estimate of the overall flux (see Section 5.1).

Most of the spectra observed during the impulsive phase are well represented by a thermal component (dark blue in Figure 8) plus a single power-law component (light blue), describing the electron bremsstrahlung emission in the 10–200 keV range. During the strongest HXR intensity peaks, however, the spectral fit procedure can at times return somewhat ambiguous results because multiple solutions can be obtained for the same spectra. A major cause of this ambiguity is the balance between thermal and nonthermal components that can be assigned in the final spectral characterization. For this reason, our approach has been to derive the electron temperature from simultaneous GOES observations (see White et al. 2005), thus better constraining the thermal component. In general, the δ spectral index is well characterized in the fits, while the estimate of the power contained in the nonthermal electrons strongly depends on the total flux of nonthermal electrons and the low-energy cutoff value. Better constraining the temperature in this case provides a more realistic estimate of the low-energy cutoff, which is critical for the modeling (see Section 6).

The evolution of the model parameters derived from the fits are shown in Figure 9 for an 8-minute interval during the flare's impulsive phase. Given that the IRIS data are acquired with a 9.4 s cadence, after fitting all the spectra at their original time resolution of 1 s, we calculated the mean and the rms of the spectral parameters over 10 s intervals, assuming that the dispersion of their values mostly represents the uncertainties of the fitting procedure rather than a real evolution of the spectra within 10 s. The short vertical bars in Figure 9 indicate the range of variation for each parameter in these intervals. The dashed lines, also outlined in Figure 3, frame the period of maximum UV emission and condensation flows for the flaring pixels sampled by the IRIS slit. Figure 9 reveals fairly hard spectra with $\delta \approx 5$, in particular, during the first intensity peak phase around 17:27–17:28 UT (see Figure 3). The nonthermal electron power, however, reaches its maximum of $P_{nth} \approx (2\text{–}3) \times 10^{29}$ erg s^{-1} within the 17:29–17:31 interval, which corresponds to the maximum emission in the IRIS channels. This is also the interval when maximum flux is inferred, as described in the next section.

Finally, using the derived values of nonthermal electron power integrated over the whole flare duration (from 17:20:16 to 17:51:00, i.e., significantly longer than the interval shown in Figure 9), we estimate a total energy content in the accelerated electrons of about 10^{32} erg. This is broadly consistent with the values reported in the literature for large eruptive flares, e.g., Emslie et al. (2012).

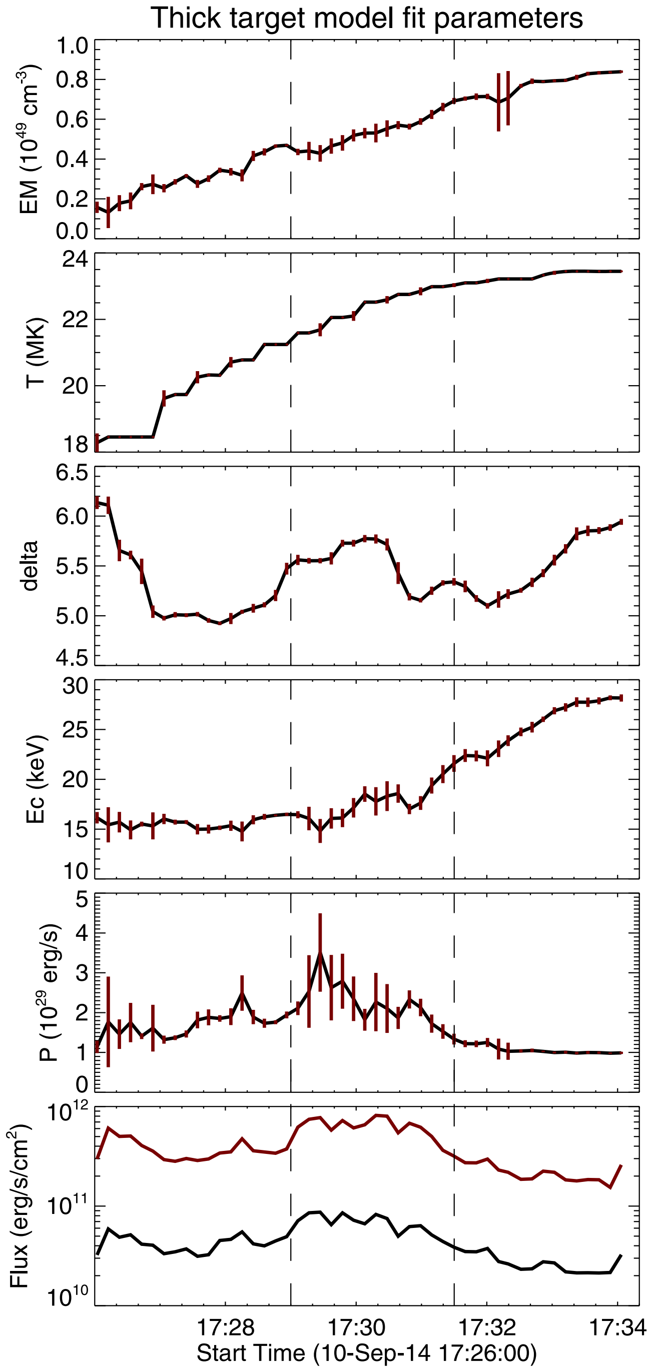

Figure 9. Time profile of the HXR spectral parameters obtained from the fits of Fermi spectra at 1 s cadence. Values shown are averaged over 10 s; vertical brown bars represent the variations over such intervals (some bars are so small that they are hidden in the plot). From top to bottom: emission measure and electron temperature of the thermal component; spectral index δ, cutoff energy and total power of the nonthermal electron energy distribution; nonthermal electron flux. The latter requires an estimate of the area involved in the HXR emission, as described in Section 5.

5. Area and Duration of Energy Release Episodes

The spatially unresolved Fermi observations are ill-suited to estimate two parameters crucial to a full description of the electron beam: the energy flux (erg s^{-1} cm^{-2}) impinging on the chromosphere, which depends on the (time-varying) area involved, and the duration of this energy input in any given area. These values can be derived from RHESSI combined imaging and spectroscopy when available; even so, they often suffer from large uncertainties due to poor spatial and temporal resolution, or noise in the data. For this reason, it has become customary to estimate the area impinged on by the electron precipitation directly from the size of optical and UV chromospheric brightenings (e.g., Krucker et al. 2011; Kowalski et al. 2015, 2017a; Kuridze et al. 2015).

The duration of each energy-deposition episode is instead estimated using various techniques, including the rising time of the UV brightness of individual kernels (Qiu et al. 2010, 2012), the duration of "single" bursts in the HXR (or derivative of SXR) curves (Cauzzi et al. 1995, 1996; Rubio da Costa et al. 2016), or the comparison of coronal diagnostics with multi-thread modeling, employing the duration as a free parameter (Warren 2006). In the following we attempt to provide realistic estimates for these two beam parameters for the case of SOL2014-09-10T17:45 using the concomitant Fermi, IRIS, and AIA observations.

5.1. HXR Energy Flux

The close temporal correlation of HXR and UV emission during flares has long been recognized (see, e.g., Cheng et al. 1981, 1988), and is generally understood in terms of both signatures being produced by the impulsive heating of the lower atmosphere from precipitating nonthermal electrons. Observations with higher spatial resolution have clarified, however, that the global UV emission curves result from the staggered occurrence of multiple flaring kernels, each one displaying a similar evolution of the UV emission, with a rapidly rising phase and a much longer cooling decay (Qiu et al. 2010, 2012, see also Figure 12 below). Details of the actual energy deposition are encoded mainly in the rising phase of such "individual" curves.

We exploit this property of the UV emission by computing the running difference of the IRIS 2796 Å SJIs at their original cadence of 19 s, with the idea that every flaring area undergoing heating would be clearly recognized in such difference images (the 1400 Å images could not be used because they are overly saturated). Figure 10 shows the difference images for four representative times during the flare development; only the positive intensity changes from the prior image are displayed using an inverted color table with logarithmic scaling; a threshold is used to remove the background noise. Every structure visible in the images represents an area that is either newly activated or still in the rising phase of the UV curve—hence still experiencing energy input at that given moment. Two contour levels are shown in the difference images: the most intense regions are defined at a change of more than 130 DN, containing between 40% and 50% of the total intensity change in each image, and they are displayed in green, while the weaker enhancements of the ribbon chromosphere are shown in black at a level of 9 DN, approximately five times the noise—as determined from the average counts in an area free of ribbon emission in the bottom left corner.

For any given time, we computed the area of the flaring sources from the total number of new pixels within each of these contours. Note that a further correction is required to take into account the small part of the ribbon area that is not imaged by IRIS SJIs (see Figure 1); to this end, we introduce a factor determined from the ribbon area at the 2000 DN level in the AIA 1600 Å image acquired closest in time. In the 17:20 and 17:50 UT interval this factor varies between 1.0 and 1.2.

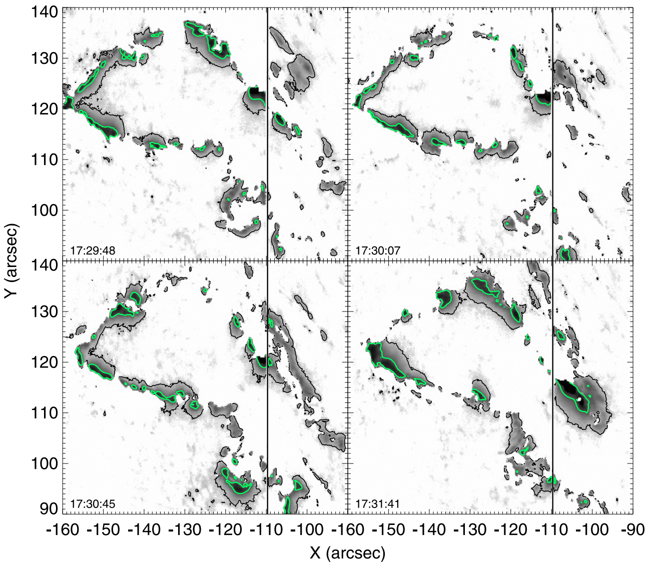

Figure 10. Positive running difference of SJI 2796 Å images for four representative times during the flare development (inverted, log intensity scale). Green and black contours represent a 130 and 9 DN intensity change, respectively. A reduced FOV surrounding the most intense part of the flare ribbon is shown (see Figure 1); the IRIS slit is visible as the black line.

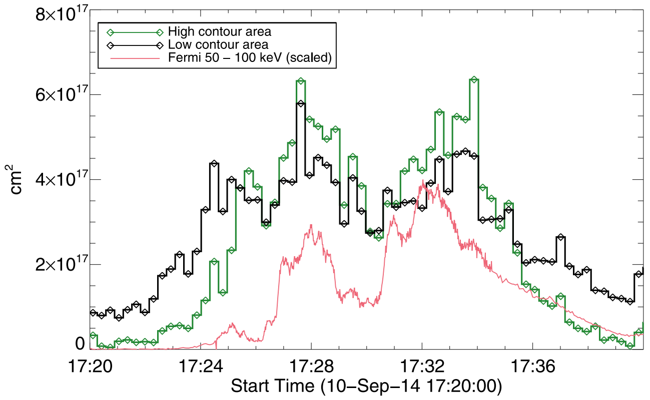

Figure 11. Newly activated kernel area in comparison with the Fermi 50–100 keV light curve (normalized and scaled to the plot window). The area was taken from 2796 Å SJIs at the level of the green and black contours in Figure 10 and includes a correction for the missing ribbon area seen in the AIA 1600 Å images.

A strong correlation exists between the "active" ribbon area and the HXR emission. This is apparent in Figure 11, where the area (in cm^2) calculated from the strongest contours of Figure 10 is plotted alongside the 50–100 keV emission from Fermi. In particular, during the central portion of the impulsive phase of the flare (17:26:30–17:32:30 UT), most HXR bursts correspond to new peaks in the area curve. The relationship is tight in the temporal sense, but not in amplitude: at times, relatively modest enhancements in the HXR emission might correspond to large increases in area (see the interval 17:29–17:30 UT), while at other times, the opposite occurs (interval 17:30:30–17:31:30 UT). The main point of Figure 11 is then a confirmation of the results of Qiu et al. (2010, 2012) reported above, i.e., that the UV emission in any given area can be meaningfully correlated with the HXR signal, as an indication of accelerated electrons impacting the chromosphere, only during its rising phase.

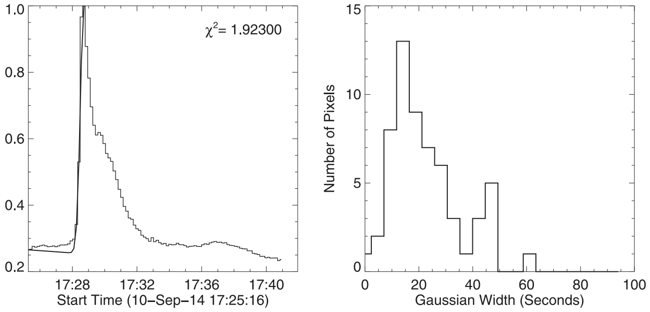

Figure 12. Left panel: example light curve of normalized Fe II 2814.45 Å intensity (stepped line) with a Gaussian fit (smooth line) to the data prior to the peak; the same pixel as in Figure 5. Right panel: histogram of fitted Gaussian widths in seconds for fits with reduced $\chi^2 \geqslant 0.5$ and $\chi^2 \leqslant 5$.

An average beam energy flux at any given time during the flare can be estimated using the flaring area values calculated above. Given the temporal evolution of the power in the nonthermal electrons as derived in the previous section and the two area limits as described above, we find the lower and upper limit to the average flux to be on the order of $\approx 10^{11}$–10^{12} erg cm^{-2} s^{-1}, shown in the bottom panel of Figure 9. These are rather high fluxes, at the limit of what current radiative-hydrodynamical simulations assume for typical solar flaring conditions. Flux values on the order of several 10^{11} erg cm^{-2} s^{-1} are also derived in recent papers, however, that use high spatial resolution UV and optical data (Krucker et al. 2011; Kennedy et al. 2015; Kuridze et al. 2015; Kowalski et al. 2017a, 2019).

From the curves of Figure 11 we realize that there is no obvious reason for the HXR spectrum to be self-similar in each flaring kernel at any given time, so injection energy rates could be widely different from the spatial averages just derived. However, during the interval most relevant for our analysis (17:29:48–17:31:41 UT), the flaring area directly sampled by the IRIS slit was the brightest UV emitter, and as mentioned in Section 2, its intensity accounted for 15%–20% of the total 2796 Å SJI counts but for only ~1% of the total area. For this reason, a flux value of a few $\times 10^{11}$ erg cm^{-2} s^{-1} is probably a reasonable assumption, although higher fluxes cannot be excluded.

5.2. Duration of Energy Release

Figures 10 and 11 both highlight that each HXR bursts might pertain to multiple separate locations that rapidly evolve during the flare development. Because the duration of heating in any one of these ribbon pixels cannot be directly determined without spatially resolved HXR imaging, we use the UV light curve as a proxy, as mentioned above.

Shown in Figure 12 is an example of a single-pixel light curve of the total Fe II 2814.45 Å line intensity (a sum of the spectrum between 2814.24 and 2815.0 Å). Following Qiu et al. (2012), we fit the rise side of each pixel's light curve from background to peak intensity with a Gaussian profile, and assume its full Gaussian width as the heating time for that pixel.

Most of the 81 flaring pixels return a good fit, but to determine an average heating time, we consider only pixels with a reduced χ^2 between 0.5 and 5. A histogram of the relevant Gaussian widths is shown in units of seconds in the right-hand panel of Figure 12. The median width is ~22 s, with the peak in the histogram around 15 s. We therefore assume a heating duration of ~20 s in our modeling. This is consistent with the recent work of Rubio da Costa et al. (2016) and Kowalski et al. (2017a), who also analyzed high-resolution IRIS spectra of an X-class flare.

6. Model

6.1. Initial Setup

We modeled the impulsive phase of the SOL2014-09-10T17:45 event using the RADYN flare code (Carlsson & Stein 1997; Allred et al. 2015). The code solves the time-independent Fokker–Planck (F–P) equation for a prescribed injected particle beam distribution, given the charge and mass of the beam particle, the initial pitch-angle distribution in the downward hemisphere, the power-law index, the low-energy cutoff value, and the energy flux density at the top of a model 1D magnetic loop consisting of a photosphere, chromosphere, and corona.

Following the analysis of Sections 4 and 5.1, we use a flare model with the following electron beam parameters: $\delta = 5$, $E_c = 15$ keV, and energy flux of 10^{11} erg cm^{-2} s^{-1} (F11). The energy input lasted 20 s. The model QS.SL.HT of Allred et al. (2015) was used for the preflare atmosphere because it was closest to the observed plage environment. Several improvements have been made to the RADYN flare code since Allred et al. (2015), which are worth noting here (they will be described further in J. C. Allred et al. 2020, in preparation). The hydrogen broadenings from Kowalski et al. (2017b) and Tremblay & Bergeron (2009) have been included in the dynamic simulations (A. Kowalski et al. 2020, in preparation). The QS.SL.HT model was relaxed with this new hydrogen broadening, and we choose to use the X-ray back-heating formulation from Allred et al. (2005) for these models; the resulting preflare apex temperature is 1.8 MK, with an electron density of 5.1×10^9 cm^{-3}. Finally, we used a new version of the F–P solver, which gives a moderately smoother electron beam energy-deposition profile over height in the upper chromosphere.

To properly compare the model results with the observations, we then synthesized the Fe II 2814.45 Å line at different times within the evolution of the flare. As shown by Kowalski et al. (2017a, 2019), this line is an important diagnostic in flares because the intensity originates from a similar temperature range, with a broad peak around $T \sim 12{,}000$ K, as the hydrogen Balmer bound–free radiation that dominates the IRIS NUV spectral range. Furthermore, the line can be efficiently synthesized in local thermal equilibrium (LTE) using snapshots of the nonequilibrium ionization, electron density, and velocity stratification from RADYN (Kowalski et al. 2017a), and non-LTE temperature. Stronger optically thick lines, including the Mg II triplet lines, require a more careful treatment, which is beyond the scope of this paper (see, e.g., Zhu et al. 2019).

The calculation of Fe II profiles remains the same as in Kowalski et al. (2017a), except that we account for the upper photospheric ($z < 150$ km) Mg II wing opacity in LTE. This provides a more accurate contrast of the chromospheric flare radiation against the upper photospheric (nonflaring) emission. This is important for assessing faint line emission from the chromosphere, such as the Fe II line. Zhu et al. (2019) show that even a 30 times increase in the expected Stark broadening of the Mg II line produces very little wing emission at

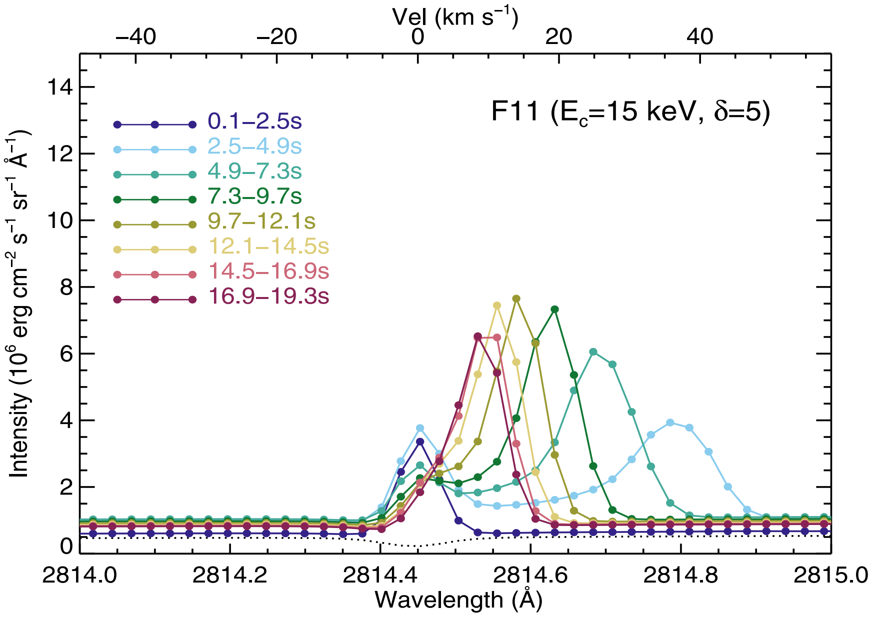

Figure 13. Synthetic spectra of Fe II 2814.45 Å obtained at different times during the evolution of the model flare. The profiles are averaged over the duration of the single IRIS exposure, i.e., 2.4 s. The dotted black line represents the preflare profile.

wavelengths >2806Å in the flare chromosphere (see Figure 4 (a) in Kowalski et al. 2019), thus we expect minimal influence in the Fe II window. Finally, for simplicity, a microturbulence parameter was not included in the broadening prescription of the Fe II 2814.45 Å line.

6.2. Model Results

Using the prescriptions described above, we calculated the spectra of the Fe II 2814.45 Å line at every 0.1 s in the simulations, and averaged them over the exposure time of the NUV IRIS data during the flare, i.e., 2.4 s. The resulting spectra are displayed in Figure 13 for the whole duration of the impulsive phase, i.e., 20 s. The preflare intensity is not subtracted and is shown as a thin dotted black line. During the whole evolution, the Fe II 2814.45 Å line (both components, see below) remains optically thin, as was the case for the flare described in Kowalski et al. (2017a).

Several important observational features appear to be reproduced by the model. First, the modeled continuum intensity varies from a preflare value of ∼0.5 to a maximum value of $\sim 1 \times 10^6$ erg cm^{-2} s^{-1} sr^{-1} Å^{-1} at 10–20 s into the flare; this is in good agreement with the observed continuum value and its enhancement (see Figure 5 and Figures A1 and A3 in Appendix A). Second, the modeled Fe II 2814.45 Å line goes into emission almost instantaneously as the flare develops, and reaches a maximum intensity of $\sim 4 \times 10^6$ erg cm^{-2} s^{-1} sr^{-1} Å^{-1}, which is again consistent with the observed intensity values. Finally, the modeled spectra show the rapid development of an additional strong redshifted component to the line, corresponding to a velocity of ∼40 km s^{-1}, that appears just a few seconds into the flare. This second component evolves very rapidly and becomes dominant with respect to the stationary component (still in emission) while decelerating at the same time: only 10 s after its first appearance, its velocity had decreased to ∼10 km s^{-1}.

The existence of a second redshifted spectral component and its dynamical evolution resemble the behavior displayed by the observed IRIS spectral lines well (Figures 4 and 5). A similar dynamical evolution of the Fe II line has been discussed by Kowalski et al. (2017a) for the case of a stronger flare (5F11, $\delta = 4.2$), and has been explained there with the development of strong chromospheric condensation (see Section 7 below); however, our data allow a more detailed comparison with the whole condensation evolution because of their high cadence and the availability of multiple flaring kernels that are observed continuously from the earliest stages.

Some discrepancies remain between the data and the modeled spectra that might point to necessary modifications of the models and/or the spectral synthesis. From the dynamical point of view, the evolution of the synthetic line intensity, especially that of the redshifted component, appears appreciably faster than in the observations. In Figure 13 the redshifted component appears just a few seconds after the heating starts, with an intensity comparable to that of the stationary component. The data, on the other hand, show a more gradual enhancement of both the stationary and redshifted components, with the latter matching the stationary component intensity only over ∼30 s. The deceleration of the redshifted component in the data also appears to be slower than in the model, with a typical decay time of ∼30 s (Figure 7) versus the ∼10 s of the simulations. Finally, the data show a buildup (over a period of 10–20 s) toward the maximum redshift, which is at odds with the instantaneous appearance of the second component in the simulated spectral profiles; this effect is better visible for the stronger lines such as Mg II and C I (Figure 7). This could merit further investigation in the context of flare precursors that are often reported (e.g., Bamba et al. 2017).

The intensity of the second component relative to the stationary one also appears higher in the synthesized lines than in the observations (see Figure 5), with instances of the synthetic redshifted component being about twice the observed one. This might be related to another discrepancy, namely that the width of the synthetic lines remains significantly smaller than observed, especially for the redshifted component, even when van der Waals and quadratic Stark broadening is accounted for in the calculation

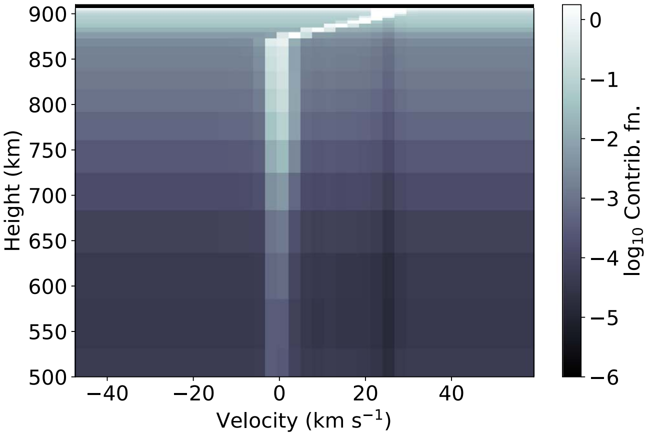

Figure 14. Contribution function (in units of erg cm^{-2} s^{-1} sr^{-1} Å^{-1} cm^{-1}) of the Fe II 2814.45 Å line at 6.5 s within the development of the flare. The *x*-axis is given in units of velocity rather than wavelength. The chromospheric condensation is clearly visible in the upper part of the graph, from $h \sim 870$–900 km, as the locus of a much enhanced contribution function at longer wavelengths, which gives rise to the redshifted component.

(opacity broadening is naturally included in the LTE line synthesis). Because the simulations do not include a microturbulence parameter or reproduce the full range of strong flare-induced turbulent motions in the chromosphere (Milligan 2011), it is plausible that the flare energy is redistributed into line profiles of higher intensity that are more narrow, however.

7. Discussion

Using the complete description of the physical properties within the simulated flaring atmosphere, we can investigate the origin of the most distinctive observational feature reported above, namely the presence of two separate spectral components for the Fe II 2814.45 Å line, each with very different dynamical behavior. Following the discussion of Kowalski et al. (2017a), we confirm that these features are due to the concomitant action of accelerated electrons of different energy impinging on the chromosphere. In particular, the highest energy electrons in our simulated beam ($E > 50$ keV, increasing to $E > 80$ keV later in the flare evolution) penetrate the deeper denser layers of the chromosphere and rapidly heat it to temperatures ∼10,000 K, producing both an enhanced continuum emission and a strongly enhanced emission in the line ("stationary flare layers"). The bulk of the beam energy, however, resides in electrons of lower energy ($E = 15$–50 keV) that are stopped in the higher more rarefied atmosphere. This causes the development of an explosive chromospheric evaporation and its counterpart condensation, a downward-moving high-density front ($n_e \sim 2 \times 10^{14}$ cm^{-3}), with a thickness of only 30–40 km and a temperature of $T \sim 8000$–12,000 K. This layer becomes sufficiently dense so as to produce additional emission in both the continuum and the chromospheric spectral lines, resulting in a separate redshifted component that traces the downward motion of the condensation toward the stationary chromosphere and its rapid demise. Figure 14 illustrates the situation at 6.5 s within the flare development: while the stationary component (at $v = 0$ km s^{-1}) is formed within ∼200 km in the mid-chromosphere, a very strong contribution appears in the condensation, concentrated in the upper 30–40 km of the atmosphere, at the redshifted position of $v \sim 30$ km s^{-1}. From the simulations, we find that this moving dense front lasts only a few tens of seconds because it impacts onto the stationary chromosphere of ever increasing density.

The parameters of the beam of accelerated electrons are obviously related with observable quantities, with the energy cutoff E_c, spectral index δ, and total flux F all playing different roles in the creation of the chromospheric signatures, and of the chromospheric condensation in particular (e.g., Reep et al. 2015). For the case of our flare, as discussed in Sections 4 and 5, in the thick-target approximation, the spectral index of the beam is rather well determined, while the low-energy cutoff might vary between 15 and 25 keV; the total flux of nonthermal electrons is also determined within about an order of magnitude (see Figure 9). As an additional check, we thus ran some further models, in which we kept the spectral index of the beam ($\delta = 5$) and the heating duration (20 s) constant while we varied the low-energy cutoff ($E_c = 15$, 18, 20, 25 keV) and the total flux ($F = 1$, 5×10^{11} erg cm^{-2} s^{-1}; F11, 5F11). The Fe II 2814.45 Å line was then synthesized as described in the previous section.

None of the additional models reproduced the data as closely as the model shown in Figure 13, reinforcing the case for an electron beam with a relatively low value of E_c and a moderate flux. In particular, for the models with higher cutoff energy E_c (20–25 keV), the condensation becomes notably weaker, and develops later, with respect to what observed. On the other hand, a higher beam flux (5F11) produces not only a much stronger condensation, but also a much higher continuum value than observed (a factor of several), already in the very early instants of the flare.

The combined diagnostics provided by the continuum intensity in the Fe II line spectral range, and the strength of the condensation, appears thus to be particularly valuable in constraining the model parameters (note that the continuum near the Mg II lines can usually be determined with much less precision because the wings of the line are very extended). Still, the intensity of the second component remains much higher than that of the stationary component, regardless of the different E_c values, for both the F11 and 5F11 beams. As discussed in the previous section, this is not consistent with observational data; further investigation is necessary to determine the source of this discrepancy.

8. Summary and Conclusions

Expanding on our previous work (Graham & Cauzzi 2015, Paper I), we have studied the details of chromospheric dynamics during the impulsive phase of the X1.6 SOL2014-09-10T17:45 event by employing a comprehensive set of observations and modeling. In particular, the unique set of observations obtained by IRIS allowed us an unprecedented view of the early impulsive phases of the flare, with large spectral coverage, high cadence (9.4 s), and high spatial resolution (<1″). A novel approach pursued in this work is the use of multiple chromospheric diagnostics available in IRIS spectra, including some weak Fe I and Fe II lines that are seldom employed. These lines go into clear emission in strong ribbon kernels, but never saturate, in contrast to other diagnostics such as the widely used Mg II lines. Furthermore, the Fe lines remain optically thin during the flare development, which simplifies their interpretation.

Our main findings are as follows:

1. Using several diverse spectral lines (Figures 5, 6, and A1–A4), we confirm that the chromospheric dynamics in the impulsive phase of this flare appears identically in multiple independent flaring kernels that develop at successive times, separated by as much as several minutes and $\sim 10''$ (Figure 4, bottom panel). This represents a best-case scenario for comparison with (1D) numerical models of flaring loops.
2. In the earliest instants of activation for any given flaring kernel, all the chromospheric lines show a clear double-component structure, with an enhanced spectral line centered at the rest wavelength, and a strongly redshifted component at $\Delta\lambda \sim 40\,\mathrm{km\,s^{-1}}$. Their relative intensities and position evolve within a few tens of seconds, with the reshifted component rapidly decelerating until the two components merge in an apparently single, very broad, and asymmetric line. Such a behavior had been observed sporadically before (Tian et al. 2015), but was never reported so comprehensively during its complete evolution.
3. The temporal evolution of the redshifted component appears very similar for all spectral lines and all flaring kernels (Figure 7), with a timescale of ~ 30 s. This behavior is consistent with the presence of a strong chromospheric condensation, as first modeled by Fisher et al. (1985) and Neidig & Machado (1986).
4. Adopting the standard thick-target approach, we use cotemporary HXR observations by the Fermi satellite as well as relevant IRIS diagnostics to derive the parameters of a beam of accelerated electrons impinging on the chromosphere. While the beam is not particularly hard ($\delta = 5$), we find both a low-energy cutoff value ($E_c \sim$ 15–20 keV) and a fairly high flux ($F = 10^{11}\,\mathrm{erg\,s^{-1}\,cm^{-2}}$), which combine into a strong heating of the chromosphere. Using these parameters as input to the RADYN flare code (Carlsson & Stein 1997; Allred et al. 2015), we find that the low chromosphere is rapidly heated by the highest energy electrons, while the bulk of the electron beam energy is dissipated at higher layers. The latter causes the rapid development of an explosive chromospheric evaporation and its counterpart condensation, with a maximum velocity of $\sim 50\,\mathrm{km\,s^{-1}}$. The condensation is sufficiently dense to give rise to additional continuum emission, as well as to highly redshifted components of the analyzed chromospheric lines. The downward motion of the modeled condensation lasts only a few tens of seconds.
5. To properly compare the results of the simulation with the actual data, we synthesize the Fe II 2814.45 Å line profile in different snapshots of the resulting atmosphere, averaging over time in a manner consistent with the actual IRIS exposures (see also Kowalski et al. 2017a). The synthetic Fe II profiles (Figure 13) reproduce many of the observed characteristics, including the presence of two separate spectral components and their initial separation, as well as the continuum enhancement in the Fe II window. As discussed in Section 7, the redshifted spectral component and the excess continuum are produced in the condensation described above (point 4), while the stationary component is enhanced because of the heating of the deeper layers due to the penetration of the highest energy electrons. We also find that the continuum intensity in the Fe II spectral window is an important additional constraint on the details of the energy release because it is rather sensitive to the beam parameters (Section 7). The main inconsistencies between the model and the data include a faster temporal evolution, a higher relative intensity, and a reduced width of the redshifted component in the simulations with respect to observations. This could be further investigated by adopting a different initial atmosphere in the simulation, and analyzing the possible role of turbulent flows in the chromospheric condensation, which might influence both the width and intensity of the reshifted component (see Section 7).
6. For some flaring kernels there are indications of a short "buildup" phase toward the maximum redshift of the condensation component, which is well visible in the Mg II 2791.6 Å panel of Figure 7. This is not predicted by the hydrodynamical simulations and might be related to the details of a "precursor" phase observed in some instances. However, we did not perform a systematic analysis of the possible effects of noise and/or the instrumental PSF in producing this signature. Recently, using a time-dependent nonequilibrium approach to calculate the atomic level populations, Kerr et al. (2019b) have shown that the Mg II k line becomes slightly redshifted before the impulsive condensation response (their Figure 2(a)). This could be an interesting avenue of further investigation.

As a final curiosity, the slight and short-lived blueshift visible in Figure 4 after the condensation dies down appears to represent a rebound of the stationary chromosphere after it is hit by the condensation, and is reproduced in some RHD simulations like those of Reep et al. (2016, their Figure 2).

We conclude by remarking that the combination of multiple diagnostics, including HXR emission, UV spectra and continuum intensities, and UV imaging, as well as their temporal evolution, allowed us to strongly constrain the heating and hydrodynamical properties of the impulsive phase of the SOL2014-09-10T17:45 flare. The excellent agreement between multiple observed spectral properties and the results of the 1D RHD simulations strongly suggests that for this flare, we are close to spatially and temporally resolving the impulsive phase of elementary flare kernels, each one occurring in previously undisturbed chromospheric areas. In particular, our data do not appear to require any multithread scenario of the kind often invoked to explain various flare characteristics, including how the chromospheric emission and/or dynamics of spatially resolved flare footpoints can proceed for an evidently much longer time than predicted by impulsive heating models (e.g., Qiu & Longcope 2016; Reep et al. 2016).

In our study, however, we focused exclusively on the earliest moments of the energization of the chromosphere caused by a strong electron beam (energy flux $\sim 10^{11}\,\mathrm{erg\,cm^{-2}\,s^{-1}}$), and the resulting classical explosive evaporation scenario as described by Fisher (1989). For the longer term chromospheric response, we note that the curves of integrated emission of the Fe II line described in Section 5.2 and Figure 12 are tantalizingly similar to the AIA 1600 Å curves shown by Qiu et al. (2012) for a different flare (but with a vastly different timescale, over 10 times shorter), both showing a sharp peak and a much extended "gradual" phase, although new work suggests that care should be taken in interpreting the AIA 1600 Å channel

(Simões et al. 2019). Whether this behavior is due to the normal cooling of the atmosphere after the flaring episode or to a two-stage heating process as discussed by Qiu & Longcope (2016) will be investigated in a future research.

The research leading to these results has received funding from the European Community's Seventh Framework Programme (FP7/2007-2013) under grant agreement No. 606862 (F-CHROMA). D.G. acknowledges support by NASA under contract NNG09FA40C (IRIS). A.F.K. acknowledges support from NASA Helio GI grant NNX17AD62G. P.J.S. has received funding from FAPESP (grant 2013/24155-3). IRIS is a NASA small explorer mission developed and operated by LMSAL with mission operations executed at NASA Ames Research center and major contributions to downlink communications funded by the Norwegian Space Center (NSC, Norway) through an ESA PRODEX contract. The National Solar Observatory (NSO) is operated by the Association of Universities for Research in Astronomy, Inc. (AURA), under cooperative agreement with the National Science Foundation. The article benefited from discussions at the International Space Science Institute (ISSI) during a meeting "Magnetic Waves in Solar Flares: Beyond the Standard Flare Model." Several of the plots use the colorblind-friendly tables provided by Wright (2017).

Appendix A
Additional Spectra

The spectra shown in Figures 5 and 6 illustrate a particularly clear example of the presence of a redshifted component and its temporal evolution during the impulsive phase of the flare, but are well representative of many flaring positions along the slit. To support the analysis of Section 3.1, we show in Figures A1–A4 the corresponding spectra for two additional pixel locations, marked by blue diamonds in the bottom panel of Figure 4. Each spectral range is shown for five consecutive times starting from the impulsive rise (note the different activation times in different pixels), and displays the formation of the red satellite component and its migration back toward the rest component well. The samples are taken from 3$''$.3 and 2$''$.7 above and below the spectra of Figures 5 and 6—beyond the influence of the PSF described in Appendix B below.

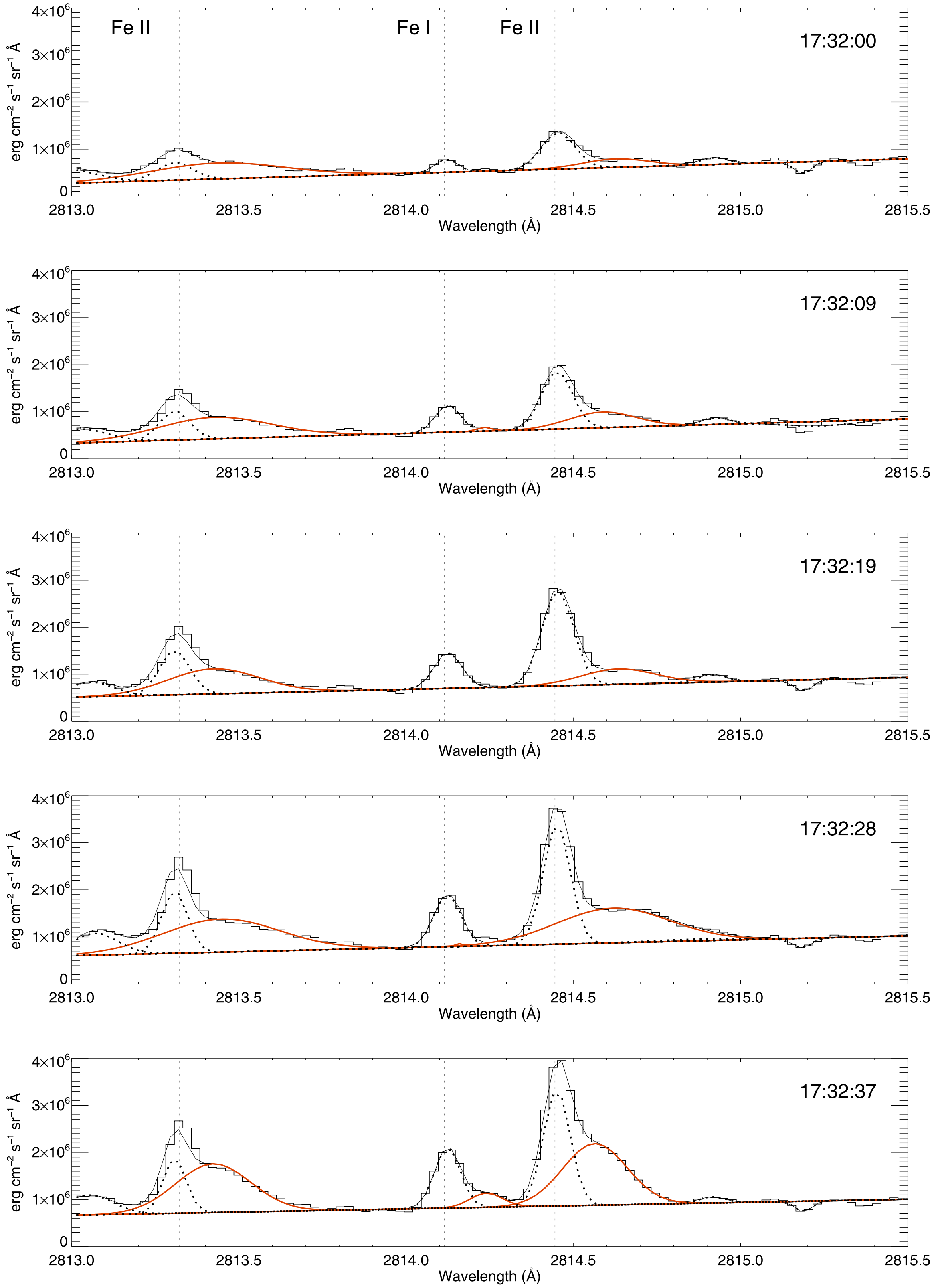

Figure A1. Fe II window for multiple chromospheric lines (stepped black lines) for the $y = 116\farcs86$ slit pixel. Labels are the same as in Figure 5.

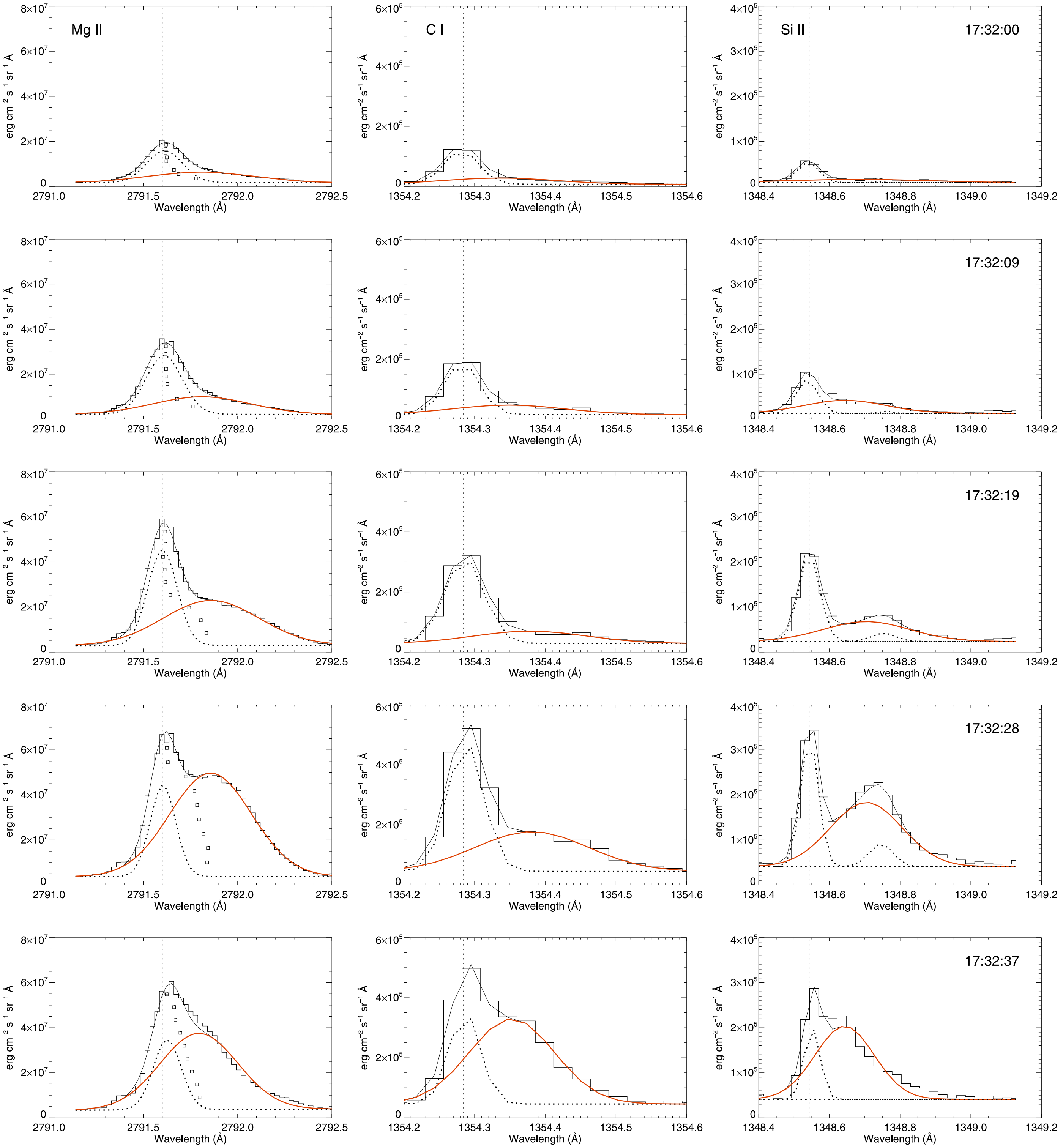

Figure A2. Spectra for the Mg II, C I, and Si II lines at $y = 116''.86$ slit pixel. Labels are the same as in Figure 6.

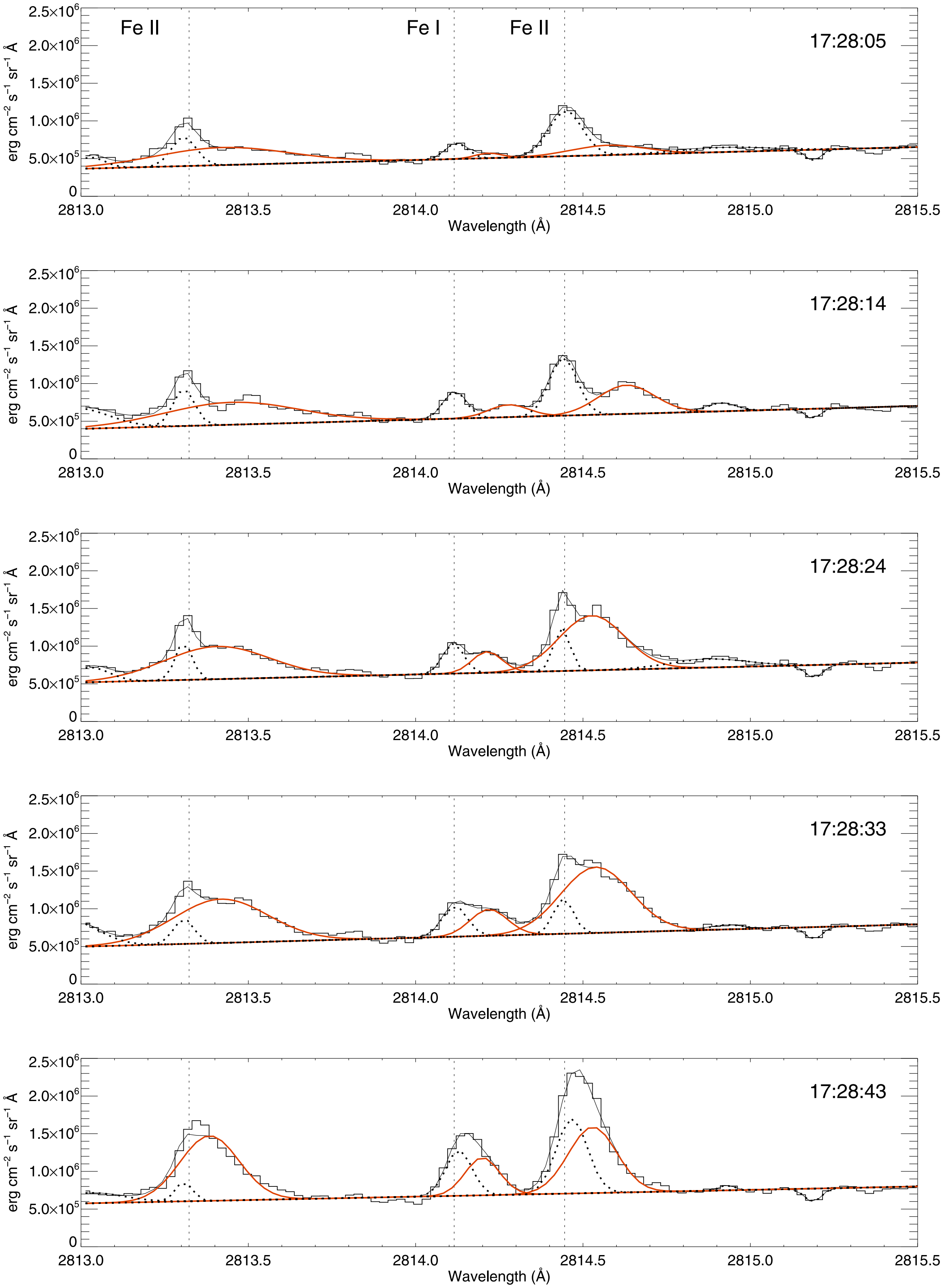

Figure A3. Fe II window for multiple chromospheric lines (stepped black lines) for the $y = 122\farcs86$ slit pixel. Labels are the same as in Figure 5.

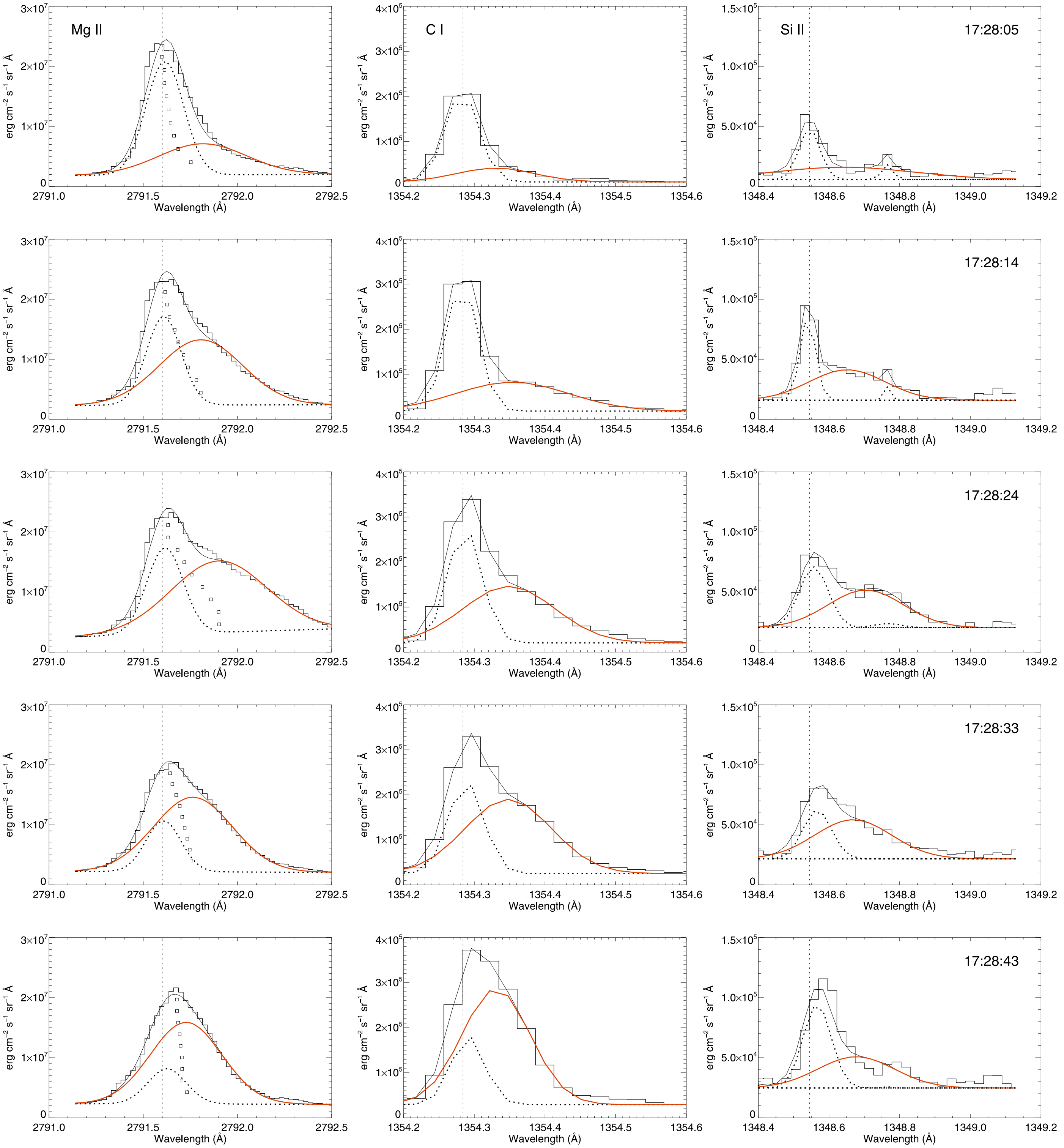

Figure A4. Spectra for the Mg II, C I, and Si II lines for the $y = 122''.86$ slit pixel. Labels are the same as in Figure 6.

Appendix B
Effects of the IRIS Point-spread Function

The progression of the ribbon(s) in the SOL2014-09-10T17:45 flare is such that the activation of separate flaring pixels along the slit occurs in a sequential fashion, thus separating in space and time the short-lived kernels, and creating the diagonal intensity streak shown in the lower panel of Figure 4.

However, one must be conscious of possible effects of the PSF of the instrument, which might alter the behavior of adjacent pixels, especially in the presence of strong intensity gradients. In particular, an intensity cross-talk along the slit might mimic the activation of a new kernel following a particularly bright kernel, or falsely prolong the duration of a flow in a previously activated pixel. Indeed, close inspection of the space–time plot in Figure 4 shows a general tendency

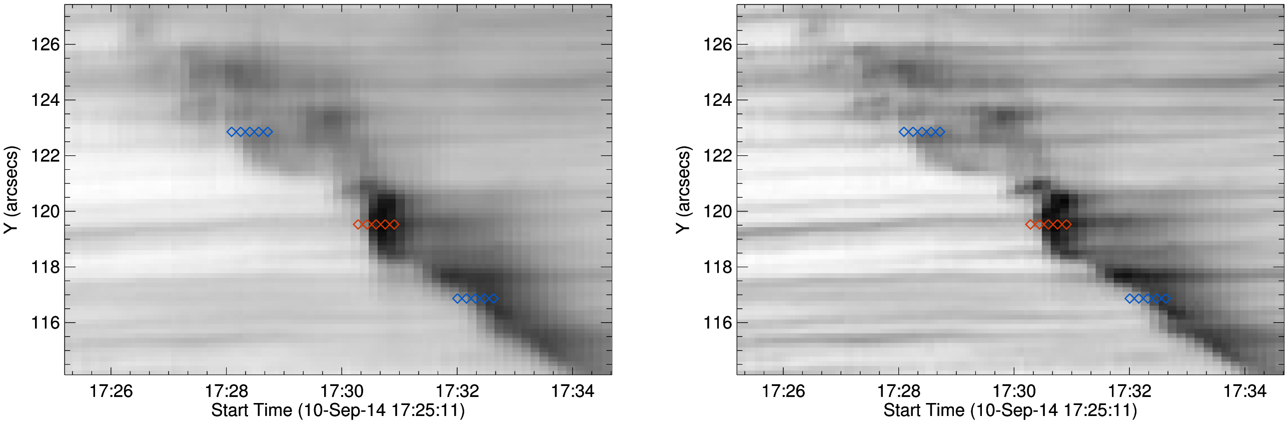

(a)

(b)

Figure B1. Space–time plots of the total Fe spectral window intensity. Panel (a) shows the unfitted observed data and Panel (b) the output from the IRIS_SG_DECONVOLVE IDL routine with 15 iterations.

to bright structures being elongated in the slit direction, an effect most apparent for ∼1″–2″ below the brightest pixels at $y = 119''$.

Alissandrakis et al. (2018) report on the straylight measured along the direction of the slit in observations of the limb, and determine an upper limit to the IRIS PSF of 0.″73 (FWHM), i.e., approx. 4–5 IRIS pixels. For the flaring kernels displayed in Figure 4, the intensity appears to spread farther than the nominal NUV spatial resolution of 0.″4 (De Pontieu et al. 2014), but the smears weaken quickly (in space) compared to the kernel core. For example, for the brightest pixel within the red diamond sequence, moving 1″ downward along the slit quickly reduces the fitted intensity of the Fe II line to 38% of the peak and to 15% when moving 2″.

Still, we attempted a correction of these effects using the deconvolution method described by Courrier et al. (2018), who took advantage of a Mercury transit to precisely determine the PSF of IRIS. Figure B1 shows the results. While the deconvolution algorithm clears some of the straylight and sharpens the resulting intensity (Panel (b)), the variations for the flaring pixels are not substantial, especially for the temporal development. More importantly, we found that the algorithm introduces additional noise in the spectral profiles, making the complex multi-Gaussian fits that we use quite unstable. Thus, rather than create a new unquantified source of error, we acknowledge that some amount of straylight may leak into the rise phase of pixels southward (lower y-values along the slit) of a strong kernel. Given the thresholds used in our fitting routines, and because spectra measured in weaker flaring kernels (including those identified with blue diamonds in Figure 4, and presented in Figures A1–4, and presented in Figures A4) are qualitatively and quantitatively very similar to those acquired in the brightest pixel, we believe that this leak has only a minor effect on our results.

Appendix C
Spectral Bisectors

As described in Section 6.2, and similar to the case discussed in Kowalski et al. (2017a), the Fe II 2814.4 Å line remains optically thin during the flare, thus justifying the use of two separate Gaussians to describe the dynamics and evolution of the different flare components. The fact that a similar analysis appears valid also for the Mg II 2791.6 Å line (see Figure 7 and Section 3.2) allows us important insights into the use of bisectors, a commonly used method for estimating the velocity of the condensation when strong optically thick lines are used.

Following the explanation of Ichimoto & Kurokawa (1984) of the Hα red-wing “excess” as due to a very broad redshifted component formed in an optically thin condensation, Canfield et al. (1990) first introduced the use of bisectors, measured in the extreme wings of that line, to derive the amplitude of the motions. In their work, Canfield et al. (1990) pointed out that the positions of the bisectors should be independent of intensity because the emission in the extreme wings would be produced only in the condensation. For most flares, however, this was not observed, with the bisector positions at low intensities usually increasing to ever longer wavelengths. For this reason, it became customary to estimate the velocity of the condensation using the maximum bisector position (Canfield et al. 1990), or the position measured at around 20%–30% of the peak line intensity (e.g., Wulser et al. 1992; Ding et al. 1995; Graham & Cauzzi 2015), but without providing sound physical reasons for this practice.[11]

The Mg II panels in Figure 6 (and Figures A2 and A4 in Appendix A) offer guidance for the analysis of optically thick flaring spectral lines. The small squares in the plots identify the bisector positions measured at 10% intensity intervals, and illustrate how the bisector positions can indeed be influenced by a complex mix of the parameters of the two spectral components, including the particular phase of the evolution at which the spectra are acquired. As a general statement, at the earliest stages of the condensation, the bisector positions will be observed to increase continuously at lower line intensities because the redshifted component is far weaker than the stationary component (top panels in the figures). On the other hand, when the intensity of the redshifted component becomes comparable to or even higher than that of the stationary component, it will dominate the signal in both wings, thus producing an intensity-independent bisector. This suggests that many of the reported odd shapes of strong chromospheric lines in flares are due to the vagaries of the observations—

---

[11] Note that neither Ichimoto & Kurokawa (1984) nor Canfield et al. (1990) commented on the strength of the stationary components and its possible variations.

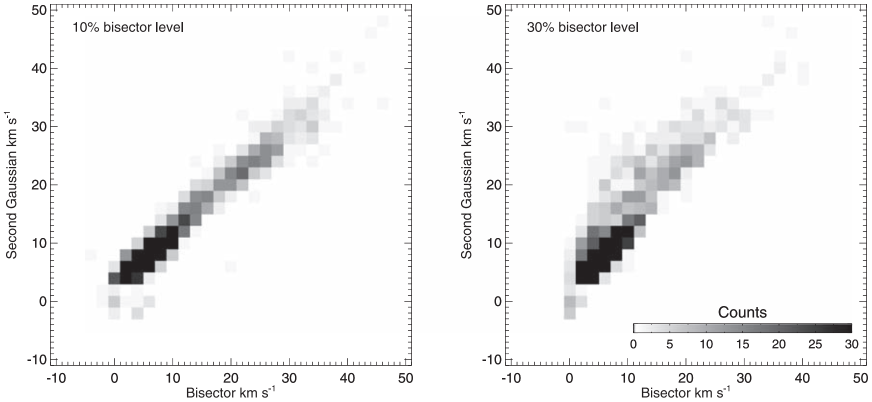

Figure C1. Chromospheric condensation velocities of the Mg II 2791.6 Å line as measured by the bisector, at 10% and 30% of the maximum profile intensity, vs. the velocity as determined by the second fitted Gaussian component. Correlations between the two quantities are 0.96 and 0.88, respectively (see the text). The same selection of fits that appear in Figure 7 is used here.

essentially, which evolutionary stage was sampled in which flaring kernel (many flare studies suffer from less than optimal cadence of the observations, e.g., Kleint et al. 2015).

Given the excellent coverage of the impulsive phase of this flare provided by the IRIS data, we are in a unique position to test the validity of the bisector method, in comparison with the actual position of the redshifted component during the flare impulsive phase. Figure C1 shows a scatterplot of the two quantities for the Mg II line, comparing the bisector position measured at 10% (left panel) and 30% of the overall maximum line intensity (right panel) with the position of the second spectral component derived from the fits. To this end, we used the same pixels and spectral fits that enter Figure 7. The gray scale provides the number of sampled spectra that fall within each 2 km s^{-1} bin.

The agreement in Figure C1 is remarkable for the bisector values measured at the 10% level, with a correlation higher than 0.95. For the 30% bisector level, the scatter becomes larger, although the correlation remains very high, at 0.88 (this is driven mostly by the low-velocity pixels, which are identified as the darker bins in the scatterplot; for the pixel/times when the measured bisector velocity is $\geqslant$20 km s^{-1}, the correlation decreases to 0.75). For higher bisector levels (not shown), the correlation with the chromospheric condensation is progressively lost. Thus, we conclude that the bisector values can provide a reasonable lower limit to the actual condensation velocities, provided they are measured at sufficiently low intensities.

Finally, we note that to date, most studies of chromospheric condensation have been conducted using strong optically thick lines such as Hα, Ca II H&K, or the Mg II h&k (among many, Wulser et al. 1992; Cauzzi et al. 1996; Falchi et al. 1997; Kleint et al. 2015; Li et al. 2015c). For such broad lines, the two spectral components will most often appear to be blended because the redshift of the condensation does not exceed the natural width of the line, thus giving the appearance of a single, broad, and very asymmetric line (see, e.g., the last two Mg II panels in Figure 6). This has led to some attempts to interpret the asymmetries as due to a depth-dependent velocity field within the flaring chromosphere (e.g., Cauzzi et al. 1996); as shown by Falchi & Mauas (2002), however, the asymmetries cannot be consistently reproduced in models assuming the formation of a single line over a large atmospheric span, even when an ad hoc velocity field in the mid-chromosphere is included. The results of our simulations offer a clear explanation of why this is the case.

ORCID iDs

Gianna Cauzzi https://orcid.org/0000-0002-6116-7301
Adam Kowalski https://orcid.org/0000-0001-7458-1176
Paulo Simões https://orcid.org/0000-0002-4819-1884
Joel Allred https://orcid.org/0000-0003-4227-6809

References

Alissandrakis, C. E., Vial, J.-C., Koukras, A., Buchlin, E., & Chane-Yook, M. 2018, SoPh, 293, 20
Allred, J. C., Hawley, S. L., Abbett, W. P., & Carlsson, M. 2005, ApJ, 630, 573
Allred, J. C., Kowalski, A. F., & Carlsson, M. 2015, ApJ, 809, 104
Bamba, Y., Lee, K.-S., Imada, S., & Kusano, K. 2017, ApJ, 840, 116
Benz, A. O. 2017, LRSP, 14, 2
Bissaldi, E., von Kienlin, A., Lichti, G., et al. 2009, ExA, 24, 47
Brosius, J. W., & Inglis, A. R. 2018, ApJ, 867, 85
Brown, J. C. 1971, SoPh, 18, 489
Canfield, R. C., Zarro, D. M., Metcalf, T. R., & Lemen, J. R. 1990, ApJ, 348, 333
Carlsson, M., & Stein, R. F. 1997, ApJ, 481, 500
Cauzzi, G., Falchi, A., Falciani, R., et al. 1995, A&A, 299, 611
Cauzzi, G., Falchi, A., Falciani, R., & Smaldone, L. A. 1996, A&A, 306, 625
Cavallini, F. 2006, SoPh, 236, 415
Cheng, C.-C., Tandberg-Hanssen, E., Bruner, E. C., et al. 1981, ApJL, 248, L39
Cheng, C.-C., Vanderveen, K., Orwig, L. E., & Tandberg-Hanssen, E. 1988, ApJ, 330, 480
Courrier, H., Kankelborg, C., De Pontieu, B., & Wülser, J.-P. 2018, SoPh, 293, 125
De Pontieu, B., Title, A. M., Lemen, J. R., et al. 2014, SoPh, 289, 2733
Dickson, E. C. M., & Kontar, E. P. 2013, SoPh, 284, 405
Ding, M. D., Fang, C., & Huang, Y. R. 1995, SoPh, 158, 81
Dudík, J., Polito, V., Janvier, M., et al. 2016, ApJ, 823, 41
Emslie, A. G., Dennis, B. R., Shih, A. Y., et al. 2012, ApJ, 759, 71
Falchi, A., Falciani, R., & Smaldone, L. A. 1992, A&A, 256, 255
Falchi, A., & Mauas, P. J. D. 2002, A&A, 387, 678
Falchi, A., Qiu, J., & Cauzzi, G. 1997, A&A, 328, 371
Fisher, G. H. 1987, ApJ, 317, 502
Fisher, G. H. 1989, ApJ, 346, 1019
Fisher, G. H., Canfield, R. C., & McClymont, A. N. 1985, ApJ, 289, 414
Fletcher, L., Dennis, B. R., Hudson, H. S., et al. 2011, SSRv, 159, 19
Graham, D. R., & Cauzzi, G. 2015, ApJL, 807, L22
Heinzel, P., Kašparová, J., Varady, M., Karlický, M., & Moravec, Z. 2016, in IAU Symp. 320, Solar and Stellar Flares and their Effects on Planets, ed. A. G. Kosovichev, S. L. Hawley, & P. Heinzel (Cambridge: Cambridge Univ. Press), 233
Heinzel, P., & Kleint, L. 2014, ApJL, 794, L23
Heinzel, P., Kleint, L., Kašparová, J., & Krucker, S. 2017, ApJ, 847, 48
Holman, G. D., Aschwanden, M. J., Aurass, H., et al. 2011, SSRv, 159, 107

Ichimoto, K., & Kurokawa, H. 1984, SoPh, 93, 105

Jeffrey, N. L. S., Fletcher, L., Labrosse, N., & Simões, P. J. A. 2018, SciA, 4, 2794

Kennedy, M. B., Milligan, R. O., Allred, J. C., Mathioudakis, M., & Keenan, F. P. 2015, A&A, 578, A72

Kerr, G. S., Allred, J. C., & Carlsson, M. 2019a, ApJ, 883, 57

Kerr, G. S., Carlsson, M., & Allred, J. C. 2019b, ApJ, 885, 119

Kerr, G. S., Simões, P. J. A., Qiu, J., & Fletcher, L. 2015, A&A, 582, A50

Kleint, L., Battaglia, M., Reardon, K., et al. 2015, ApJ, 806, 9

Kleint, L., Heinzel, P., Judge, P., & Krucker, S. 2016, ApJ, 816, 88

Kontar, E. P., MacKinnon, A. L., Schwartz, R. A., & Brown, J. C. 2006, A&A, 446, 1157

Kowalski, A. F., Allred, J. C., Daw, A., Cauzzi, G., & Carlsson, M. 2017a, ApJ, 836, 12

Kowalski, A. F., Allred, J. C., Uitenbroek, H., et al. 2017b, ApJ, 837, 125

Kowalski, A. F., Butler, E., Daw, A. N., et al. 2019, ApJ, 878, 135

Kowalski, A. F., Cauzzi, G., & Fletcher, L. 2015, ApJ, 798, 107

Krucker, S., Hudson, H. S., Jeffrey, N. L. S., et al. 2011, ApJ, 739, 96

Kuridze, D., Mathioudakis, M., Simões, P. J. A., et al. 2015, ApJ, 813, 125

Li, D., Ning, Z. J., & Zhang, Q. M. 2015a, ApJ, 807, 72

Li, D., Ning, Z. J., & Zhang, Q. M. 2015b, ApJ, 813, 59

Li, Y., Ding, M. D., Qiu, J., & Cheng, J. X. 2015c, ApJ, 811, 7

Libbrecht, T., de la Cruz Rodríguez, J., Danilovic, S., Leenaarts, J., & Pazira, H. 2019, A&A, 621, A35

Meegan, C., Lichti, G., Bhat, P. N., et al. 2009, ApJ, 702, 791

Milligan, R. O. 2011, ApJ, 740, 70

Milligan, R. O., Kerr, G. S., Dennis, B. R., et al. 2014, ApJ, 793, 70

Namekata, K., Sakaue, T., Watanabe, K., et al. 2017, ApJ, 851, 91

Neidig, D. F., & Macho, M. E. 1986, in Symp. Sponsored by the National Solar Observatory and NASA (Sunspot, NM: National Solar Observatory), 514

Ning, Z. 2017, SoPh, 292, 11

Polito, V., Testa, P., & De Pontieu, B. 2019, ApJL, 879, L17

Qiu, J., Liu, W., Hill, N., & Kazachenko, M. 2010, ApJ, 725, 319

Qiu, J., Liu, W.-J., & Longcope, D. W. 2012, ApJ, 752, 124

Qiu, J., & Longcope, D. W. 2016, ApJ, 820, 14

Reep, J. W., Bradshaw, S. J., & Alexander, D. 2015, ApJ, 808, 177

Reep, J. W., Warren, H. P., Crump, N. A., & Simões, P. J. A. 2016, ApJ, 827, 145

Rubio da Costa, F., Kleint, L., Petrosian, V., Liu, W., & Allred, J. C. 2016, ApJ, 827, 38

Rubio da Costa, F., Kleint, L., Petrosian, V., Sainz Dalda, A., & Liu, W. 2015a, ApJ, 804, 56

Rubio da Costa, F., Liu, W., Petrosian, V., & Carlsson, M. 2015b, ApJ, 813, 133

Sandlin, G. D., Bartoe, J.-D. F., Brueckner, G. E., Tousey, R., & Vanhoosier, M. E. 1986, ApJS, 61, 801

Santangelo, N., Horstman, H., & Horstman-Moretti, E. 1973, SoPh, 29, 143

Scharmer, G. B., Narayan, G., Hillberg, T., et al. 2008, ApJL, 689, L69

Schwartz, R. A., Csillaghy, A., Tolbert, A. K., et al. 2002, SoPh, 210, 165

Shibata, K., & Magara, T. 2011, LRSP, 8, 6

Simões, P. J. A., Hudson, H. S., & Fletcher, L. 2015, SoPh, 290, 3625

Simões, P. J. A., & Kontar, E. P. 2013, A&A, 551, A135

Simões, P. J. A., Reid, H. A. S., Milligan, R. O., & Fletcher, L. 2019, ApJ, 870, 114

Tian, H., & Chen, N. H. 2018, ApJ, 856, 34

Tian, H., Young, P. R., Reeves, K. K., et al. 2015, ApJ, 811, 139

Tremblay, P. E., & Bergeron, P. 2009, ApJ, 696, 1755

Uitenbroek, H. 2001, ApJ, 557, 389

Warren, H. P. 2006, ApJ, 637, 522

White, S. M., Thomas, R. J., & Schwartz, R. A. 2005, SoPh, 227, 231

Wright, P. J. 2017, ColourBlind: A Collection of IDL Colour-blind-friendly Colour Tables, Zenodo, doi:10.5281/zenodo.840393

Wulser, J.-P., Canfield, R. C., & Zarro, D. M. 1992, ApJ, 384, 341

Zhou, G. P., Zhang, J., & Wang, J. X. 2016, ApJL, 823, L19

Zhu, Y., Kowalski, A. F., Tian, H., et al. 2019, ApJ, 879, 19